

# An Advanced Discrete Fracture Methodology for Fast, Robust, and Accurate Simulation of Energy Production from Complex Fracture Networks

S. de Hoop<sup>1</sup>, D. V. Voskov<sup>1,2</sup>, G. Bertotti<sup>1</sup>, and A. Barnhoorn<sup>1</sup>

<sup>1</sup>Delft University of Technology, Delft, the Netherlands  
<sup>2</sup>Stanford University, Stanford, United States of America

## Key Points:

- We developed an open-source preprocessing tool that can create, at the required level of accuracy, a fully conformal uniformly distributed grid for a given realistic 2D fracture network with variable aperture distributions;
- This leads to a robust way of constructing a hierarchy of DFMs for uncertainty quantification of energy production from reservoirs with natural fracture networks;
- We demonstrate the application of the developed tool with complex, realistic fracture networks;
- The proposed methodology allows us to use accurate DFM models with similar computational complexity as the EDFM approach.
- The simplified DFM representations of fracture networks still capture characteristics and flow response of real complex networks;
- A novel aperture correction procedure allows us to capture the original high fidelity connectivity and flow patterns;
- We also show that it is necessary to process the raw fracture data for topological analysis.

## 23 Abstract

24 Fracture networks are abundant in subsurface applications (e.g., geothermal energy production, CO<sub>2</sub> sequestration). Fractured reservoirs often have a very complex structure, making modeling of flow and transport in such networks slow and unstable. Consequently, this limits our ability to perform uncertainty quantification and increases development costs and environmental risks. This study provides an advanced methodology for simulation based on Discrete Fracture Model (DFM) approach. Changes to the topology of the fracture network reduce computational complexity while preserving the accuracy of the DFM approximation. The preprocessing framework results in a fully conformal, uniformly distributed grid for realistic 2D fracture networks at a required level of precision. The simplified geometry and topology of the resulting network are compared with input (i.e., unchanged) data to evaluate the preprocessing influence. The resulting mesh-related parameters, such as volume distributions and orthogonality of control volume connections, are analyzed. Furthermore, changes in fluid-flow response related to preprocessing are evaluated using a high-enthalpy two-phase flow geothermal simulator. The simplified topology directly improves meshing results and, consequently, the accuracy and efficiency of numerical simulation. The main novelty of this work is the introduction of an automatic preprocessing framework allowing us to simplify the fracture network down to required level of complexity and addition of a fracture aperture correction capable of handling heterogeneous aperture distributions, low connectivity fracture networks, and sealing fractures. The graph-based framework is fully open-source, based on graph theory, and that simplifies the topology of fractures and explicitly resolves the small-angle intersections within the fracture network. Augmenting the framework with a rigorous analysis of changes in the static and dynamic impact of the preprocessing algorithm demonstrates that, we demonstrate that explicit fracture representation can be computationally efficient, used together with maintaining computational efficiency enabling their use in large-scale uncertainty quantification studies.

## 50 Plain Language Summary

51 Fractured rocks occur naturally and are abundant in the earth's subsurface, especially in rocks that host a variety of resources, from geothermal energy to clean water. Modeling fluid flow in such systems is complex and time-consuming, increasing environmental and economic risks. We attempt to tackle this problem by introducing an advanced modeling technique that simplifies the fractures' representation while maintaining the main characteristics. The method's performance is analyzed based on changes in the geometry of the fractures and fluid flow patterns. The framework manages to significantly speed up the required time for fluid flow calculations while remaining close to the high fidelity solution (i.e., solution of unchanged fracture configuration). Because most of the parameters in subsurface-related energy applications are uncertain, many simulations have to be carried out to quantify these uncertainties. Since our framework reduces the computational time, more simulations could be executed, reducing the risks associated with the development of subsurface energy resources.

## 64 1 Introduction

65 Many subsurface energy applications (e.g., geothermal energy production) rely on accurate numerical simulations of fluid flow and mass or heat transport in fractured porous media. A large class of methods is available for numerical modeling of fracture networks. It may consist of various approaches to the homogenization of fractures network, including Dual Porosity (Barenblatt, 1960; Warren & Root, 1963) and various MINC models (Pruess & Narasimhan, 1982; Karimi-Fard et al., 2006), or different versions of Embedded Discrete Fracture Models (EDFM) starting from already classic approaches (L. Li & Lee, 2008; Hajibeygi et al., 2011) to projection-based technique (Tene et al., 2017; Hos-

73 seiniMehr et al., 2020). Some hybrid versions combining EDFM with homogenized frac-  
74 tured networks at two different scales are also exist (L. Li & Voskov, 2021).

75 Another class of model is Discrete Fracture Model (DFM), where fracture segments  
76 are described as a lower-dimensional object on the mesh. The ideas of the modern DFM  
77 approach can be found in Gureghian (1975) where Finite Element Methods (FEM) was  
78 applied, and in Helmig et al. (1997) where Finite Volume Method (FVM) was used. In  
79 modern reservoir simulation, which includes highly implicit time approximation using  
80 finite-volume discretization on unstructured grids, the DFM methodology has been in-  
81 troduced by Karimi-Fard et al. (2004). The DFM approach is often preferred in detailed  
82 geological studies due to its accuracy (Moinfar et al., 2011; Flemisch et al., 2018; Berre  
83 et al., 2019; Wong et al., 2020). DFM models typically require a high meshing accuracy  
84 to resolve the fracture networks' complex geometry, thereby drastically increasing the  
85 computational complexity and rendering them unusable for uncertainty quantification  
86 purposes (Jung et al., 2013; Nejadi et al., 2017; Spooner et al., 2021). More recently, the  
87 DFM approach in reservoir simulation has been enhanced for practical applications by  
88 fully coupling geomechanics (Garipov et al., 2016) and fracture propagation (Gallyamov  
89 et al., 2018). These complex physical processes typically require a fine modeling reso-  
90 lution to capture all the effects, further exposing the limitations of incorporating uncer-  
91 tainty quantification.

92 These limitations severely constraint the necessary low-risk, sustainable, and energy-  
93 efficient subsurface activities that are desired. One of the main factors of the consider-  
94 able computational complexity of the DFM models is the meshing artifacts (i.e., *skinny*  
95 *triangles*, *small control volume sizes*, and *a large number of degrees of freedom*) that re-  
96 sult from using conformal meshes and related convergence issues (Geiger & Matthäi, 2014;  
97 X. Li & Li, 2019; Koohbor et al., 2020). Fracture network input data is typically acquired  
98 from outcrop analysis or statistical models. In outcrop analysis, raw output, either by  
99 manual or automatic interpretation, results in difficulties for the meshing software. These  
100 meshing artifacts are highlighted in Figure 1 and are well known in the existing liter-  
101 ature (Reichenberger et al., 2006; Mustapha & Mustapha, 2007; Mallison et al., 2010;  
102 Karimi-Fard & Durlofsky, 2016; Berre et al., 2019).

103 Several preprocessing strategies have been proposed in the literature to address the  
104 challenges of constructing a conformal mesh for complex natural fracture networks. How-  
105 ever, the investigation of a numerically convergent solution after applying the prepro-  
106 cessing procedure, a thorough examination of the topology changes as a function of dis-  
107 cretization accuracy, and the application to uncertainty quantification have not been ad-  
108 equately studied. Furthermore, in most existing methods, the meshing challenges related  
109 to fracture segments intersecting at a small angle are only implicitly resolved. For ex-  
110 ample, in most studies, an algebraic constraint is used for merging nodes, but the an-  
111 gle at which *fractures* intersect is not explicitly checked. This means that some mesh-  
112 ing issues are not resolved. *Finally, in the existing fracture preprocessing methods, vari-*  
113 *ability of the fracture aperture is not taken into account.*

114 Therefore, we have developed an open-source preprocessing framework that bor-  
115 rows concepts from early work in this area (Koudina et al., 1998; Maryška et al., 2005)  
116 and more recent approaches (Mustapha & Mustapha, 2007; Mallison et al., 2010; Karimi-  
117 Fard & Durlofsky, 2016). *It differs from other graph simplification works, such as Wellman*  
118 *et al. (2009), where small (low permeable) fractures are iteratively removed.* According  
119 to prescribed algebraic constraints, our preprocessing procedure merges nodes and re-  
120 solves fractures that intersect at a significantly small angle that would otherwise intro-  
121 duce additional meshing challenges. *To capture variable aperture distribution and low*  
122 *connectivity networks, in addition to previous methodologies, an aperture correction is*  
123 *added to the method presented here.* Most of the operations are formulated using graph  
124 theory, which results in simple bookkeeping of the incidence matrix operations (West et

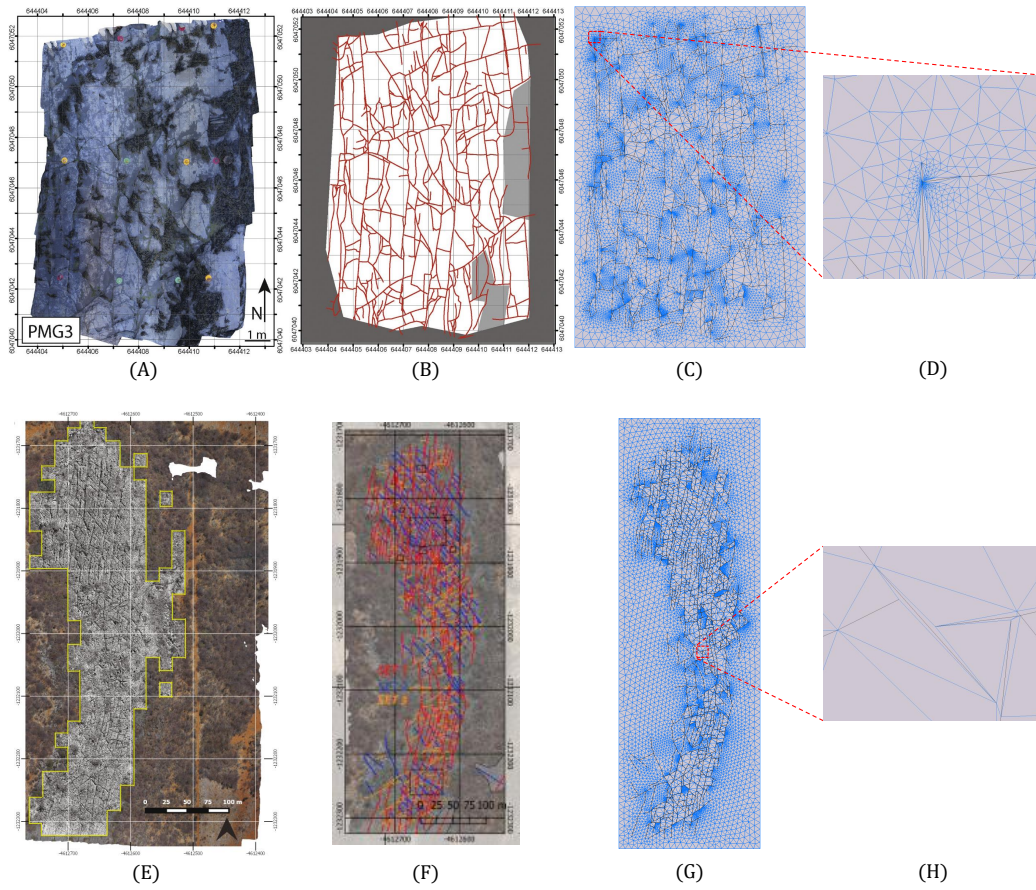


**Figure 1.** Fracture data acquisition, interpretation, and modeling steps. (A) and (E) Outcrop images obtained from the Whitby and Brejoes fieldwork area. (B) and (F) Manual interpretation of the fracture networks. (C) and (G) Conformal meshing results based on the raw interpretation. (D) and (H) is a zoom of the meshing artifacts due to complex fracture interaction. (A) and (B) Taken from Houben et al. (2017). (E) and (F) Taken from Q. Boersma et al. (2019).

al., 2001). Using the developed framework, we can create a fully conformal uniformly distributed grid based on any realistic fracture network at the required level of accuracy.

Most data obtained from outcrop studies is in planar 2D view (Bisdom et al., 2017). The available 3D data on fractures in the subsurface often consists of very coarse seismic cubes or borehole imaging logs. The attributes of the seismic cube are often too coarse to extract the exact fracture pattern, and the imaging logs only provide limited information at the well location (Q. Boersma et al., 2020). Therefore, this paper focuses on 2D fracture characterization and the preprocessing technique, which improves the meshing and subsequent fluid-flow modeling. We analyze the static and dynamic performance of the preprocessing on changes in geometry and topology of the fracture network and resulting mesh and changes in flow response. Ultimately, this leads to a robust way of constructing a hierarchy of DFMs for uncertainty quantification of natural fracture networks (de Hoop & Voskov, 2021).

Notice that the main ingredients of the developed framework and flow modeling are not limited to 2D and can be effectively applied for a fully 3D fractured networks (as shown by Karimi-Fard and Durlofsky (2016) from which we borrow several concepts). In 3D, all the fractures are represented by planes and discretized into segments (i.e., sub-planes) using an unstructured mesh. The vertices and edges of the meshed fractures will constitute the graph of the 3D fracture network, and the same preprocessing algorithm we propose in this paper (i.e., merging nodes) can be applied. Fracture apertures can be assigned to each edge of the discretized fracture, implying that the fracture aperture correction could also be used. However, some difficulties (e.g., projection of fracture aperture from the sub-plane to the edge and back) may introduce specific difficulties. A more straightforward approach could be making several slices through the 3D volume, projecting the fractures onto each slice and performing the same preprocessing on each slice (Sanderson et al., 2019).

The paper is organized as follows. We start with the description of the input data used in this study followed by the theory for preprocessing, topology analysis, and fluid flow and energy transport modeling. Next, we describe all essential ingredients of the proposed framework, including intersection, node merging, straightening, and removing acute angles. The results section contains the analysis of the static and dynamic performance of the preprocessing framework. We finish the paper with a detailed discussion and conclusion.

## 2 Materials and Methods

The accurate numerical representation of fracture networks in the subsurface is not the end goal of the modeling effort. The modeling objective is often to make better predictions on subsurface activities and their associated risks. Therefore, it is essential to test our preprocessing framework accordingly. This is done by investigating the static changes introduced by the algorithm on the dynamic behavior of the subsurface (i.e., fluid flow response). Mainly, geothermal energy production is chosen (i.e., injection of cold water and production of hot water via a well doublet) to examine this. The methodology is presented here. First, a brief description of the fracture networks used in this work is given; second is a brief introduction to graph theory; third, a brief theoretical background on the topology of fracture networks is presented; fourth, the preprocessing method is presented; fifth, the relevant equations to model the physical processes are given; and, finally, the numerical approximation of governing equations is introduced.

### 2.1 Fracture network input data

The performance of the preprocessing algorithm is examined for two realistic fracture networks, a synthetic test case, and a variable aperture distribution applied to one

of the realistic fracture networks. The first fracture network is found in the Whitby Mudstone outcrop along the cliff coast North of Whitby (UK) (Houben et al., 2017). The second example is the fracture network observed in the carbonate outcrop in Brejões, Brazil (Q. Boersma et al., 2019). Both networks are interpreted by hand; however, the developed method would also be very suitable for automatic fracture detection algorithms as presented in (Prabhakaran et al., 2019). The synthetic test case consists of a high permeable matrix and low permeable fractures with a narrow opening in the middle of the domain. The variable aperture model is applied to the Whitby fracture network (see Figure 2).

The outcrop images and the manual interpretation of the fracture networks are displayed in Figure 1. Both networks show good connectivity at first glance. The main difference between the two networks is the angle at which the fractures intersect. In the Brejoes network, this angle is around 60, while the angle is closer to 90 degrees for the Whitby network. The proposed fracture networks significantly differ in scale (Brejoes 100-1000 m vs. Whitby 1-10 m scale). Both networks are scaled up to characteristic reservoir size in a geothermal doublet system (Willems & Nick, 2019) by a scalar multiplication to preserve relative lengths and angles, which simplifies the static and dynamic analysis. The scalar is chosen for each network such that the resulting length in the y-direction is roughly 1000 [m] for both cases which is a typical distance between wells in a geothermal doublet system. Conveniently, this is a common choice for the distance between two wells in a geothermal doublet system (Willems & Nick, 2019). This scaling with a scalar multiplier can be safely done because of the fractal nature of fracture networks (i.e., the same pattern exists at several length scales) as discussed in Acuna and Yortsos (1995).

For the dynamic analysis, it is assumed that the two realistic fracture network models have very low permeability (i.e., convective flow is mainly limited by the fracture network) to ensure that the effect of changes to the fracture network on the flow response can be observed. Most fracture network data is represented through the use of shapefiles. Shapefiles are typically transformed into a data array of size  $m \times 6$ , where the first column represents the id of the primary fracture, the second column represents the id of the subsegment, the remaining four columns represent the x- and y-coordinates of the two nodes associated with the subsegment, and  $m$  corresponds to the total number of fracture subsegments. An important note is that not all manual interpretations record the intersection between all fracture segments (i.e., only the end nodes of the fractures are registered). This becomes important in the following section, where the graph is constructed based on the fracture network data. The two data arrays describing the fracture networks used in this study can be found by the following link: <https://github.com/MakeLikePaperrr/Fracture-Preprocessing-Code>.

To incorporate geological realism, a variable aperture distribution is applied to the Whitby fracture network, similar to the aperture model in Q. D. Boersma et al. (2021). The distribution and resulting apertures are visualized in Figure 2. Fractures oriented N-S are highly permeable, while fractures oriented E-W are low permeable. Figure 2 also depicts how a variable aperture leads to a much lower connectivity fracture network. Choosing a cutoff around 13% of the maximum conductivity leads to a large number of isolated fractures, hence, low connectivity.

## 2.2 Graph theory

As defined in Bollobás (2013), a graph  $G$  is an ordered pair of disjoint sets  $(V, E)$ . The set of all vertices of graph  $G$  is denoted as  $V = V(G)$ , while the set of all edges of the graph  $G$  is denoted as  $E = E(G)$ . Edges of a graph join two vertices  $i$  and  $j$  such that  $(i, j) \in E(G)$  and  $i, j \in V(G)$ . If  $(i, j) \in E(G)$ , it implies that  $i$  and  $j$  are adjacent vertices of  $G$ , and  $i$  and  $j$  are incident with the edge  $(i, j)$ .

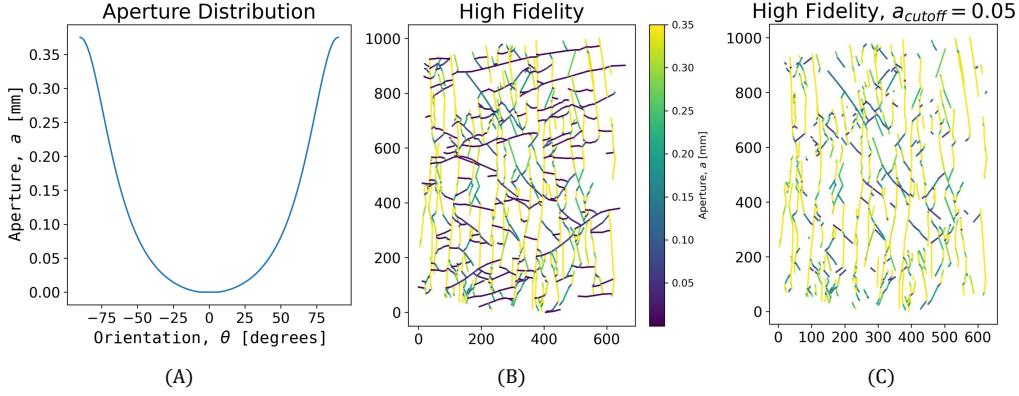


**Figure 2.** (A) and (B) Aperture distribution as a function of angle (similar to Q. D. Boersma et al. (2021)). (C) Shows only the high-permeable fractures and illustrates that variable aperture models can lead to low connectivity fracture networks.

225

Important matrix representations of the graph  $G$  are the following four matrices:

226

1. Incidence matrix:  $B(G)$ , which is a  $n \times m$  matrix, where  $n$  is the number of vertices and  $m$  the number of edges of the graph. As previously indicated, whenever a vertex  $i$  is on an edge  $(i, \cdot)$ , the vertex  $i$  is incident with edge  $(i, \cdot)$ . Hence  $B_{ij} = 1$  if vertex  $i$  is on the  $j$ -th edge otherwise  $B_{ij} = 0$ ;

227

228

229

230

231

232

233

234

2. Degree matrix:  $D(G)$ , which is a  $n \times n$  matrix describing the number of edges attached to each vertex. The degree matrix can be obtained using the following equation  $D = \text{diag}(B\mathbf{1})$ , where  $\text{diag}(\mathbf{v})$  is a function that constructs a square matrix with vector  $\mathbf{v}$  on its diagonal, and  $\mathbf{1}$  is a vector of ones with size  $m \times 1$ . The degree matrix denotes the number of edges leaving a specific vertex.

235

236

237

238

239

240

3. Adjacency matrix:  $A(G)$ , which is a square  $n \times n$  matrix, where  $n$  is the number of vertices of the graph  $G$ . As previously mentioned, if the pair of vertices  $(i, j) \in E(G)$ , they are said to be adjacent. Hence  $A_{ij} = 1$  if vertices  $i$  and  $j$  are on the edge  $(i, j)$ . Furthermore, for our purposes, it is assumed that the main diagonal is zero (i.e.,  $A_{ii} = 0$ ), which implies that no nodes are connected to itself. Note that  $A$ ,  $B$ , and  $D$  are related through the following equation  $A = BB^T - D$ .

241

242

243

244

4. Discrete Laplacian matrix:  $L(G)$  which can be found via the following equation  $L = D - A = 2D - BB^T$ . This matrix will be used for an alternative connectivity measure in the static analysis. **The Discrete Laplacian is a matrix representation of the relationships defined in a graph.**

245

246

247

248

249

250

251

252

253

254

A typical input data array  $\mathcal{F}$  that describes the fracture network contains the pairwise  $x$ - and  $y$ -coordinates of each fracture segment in the network. The first step is to convert this array into two different forms: an array that contains all the unique vertices in the graph (i.e.,  $V$ ) and the incidence matrix ( $B$ ). This is done by using Algorithm 1 which is found in the Appendix. An important assumption of this construction of  $V$  and  $B$  is that no subsegments can intersect in other places than the vertices of the particular subsegments. As mentioned before, this is often not the case in the manual interpretation of fracture networks; hence we need to calculate all possible intersections before applying Algorithm 1 shown in the Appendix. A simple intersection calculation algorithm is provided in Section 2.4.1.

255

### 2.3 The topology and geometry of fracture networks

256

257

258

259

260

261

In this section, the required mathematical relations for performing the static analysis on the effect of the preprocessing method on fracture networks are explained. Topology is used to understand how the connectivity and abutment-intersection relations of the fracture network are changing due to the preprocessing. Furthermore, it is also essential to look at how several geometrical properties of the fracture network are changing (e.g., angles and lengths) through preprocessing.

262

263

264

265

266

267

268

269

270

271

272

273

274

275

Several authors have thoroughly investigated the application of topology to fracture networks (Manzocchi, 2002; Sanderson & Nixon, 2015). Isolated nodes are typically denoted with an I, abutments are characterized by a Y-node, and X-nodes are used to indicate intersecting fracture segments. This is illustrated in Figure 3. Translating the type of nodes to the graph notation, node I is of degree one, node Y is of degree three, and node X is degree four. In general, it is unusual that more than two lines intersect at exactly one point. However, our preprocessing method merges nodes and causes several nodes to have a degree  $> 4$ . This causes us to consider all intersections of node degrees larger than four to be X type of nodes. This is used to plot the results in a ternary diagram (as shown in Figure 3). [Classifying the fracture networks topology in this way allows us to use a proxy for the connectivity. Connectivity is often defined in this context as the average number of intersections per line. This changes slightly when allowing for nodes with a degree higher than four. Instead of the definition used in Balberg and Binenbaum \(1983\)](#)

276

$$C_L = 4 \frac{N_Y + N_X}{N_I + N_Y}, \quad (1)$$

277

278

where  $N_I$  is the total number of I nodes,  $N_Y$  is the total number of Y nodes, and  $N_X$  is the total number of X nodes, we use

279

$$C_L = 2 \frac{\sum_i^d w_i N_i}{N_I + N_Y}, \quad (2)$$

280

281

282

283

284

285

286

where  $w_i$  are the weights,  $N_i$  the total number of  $i$  node types in the network, and  $i = \{Y, X, X+, X++ \dots\}$ .  $X+$  represents a vertex which is one degree higher than an  $X$  (i.e., degree five instead of four),  $X++$  two degrees higher, etc. The weights are determined by the number of lines (but not edges) involved in the vertex type (e.g.,  $N_Y$  involves two lines therefore  $w_Y = 2$  while  $N_{X++}$  involves six edges and hence three lines therefore  $w_{X++} = 3$ ). Please also note that all vertices of degree two are not used nor important in this analysis (i.e., a curved or a straight line are topologically the same).

287

288

289

290

291

292

293

294

295

An alternative connectivity measure is obtained by using the Discrete Laplacian of the graph. This matrix can be used for finding spanning trees of a given graph (i.e., connected fracture sets in the fracture network). Notably, each element of the Laplacian's null-space rational basis describes a connected component of the graph (Spielman, 2010). With this basis, we can find the number of connected fracture sets in our network and also each fracture that belongs to these components (i.e., sub-graphs). The connectivity measure is then calculated as the ratio between the cumulative length of the fractures in the largest spanning cluster and the cumulative length of all the fractures in the full network.

296

297

298

299

Geometrical properties such as angles and lengths of the fractures are obtained using simple trigonometry rules. An easy and fast way to calculate the angles of a fracture w.r.t. the x-axis is to decompose the fracture into two components (i.e.,  $\Delta x = x_2 - x_1$  and  $\Delta y = y_2 - y_1$ ). Then, the angle can be obtained using the following equation

300

$$\theta = \arctan \left( \frac{\Delta y}{\Delta x + \epsilon} \right), \quad (3)$$

301

where  $\epsilon$  is a small perturbation to prevent the case of  $\Delta x = 0$ .

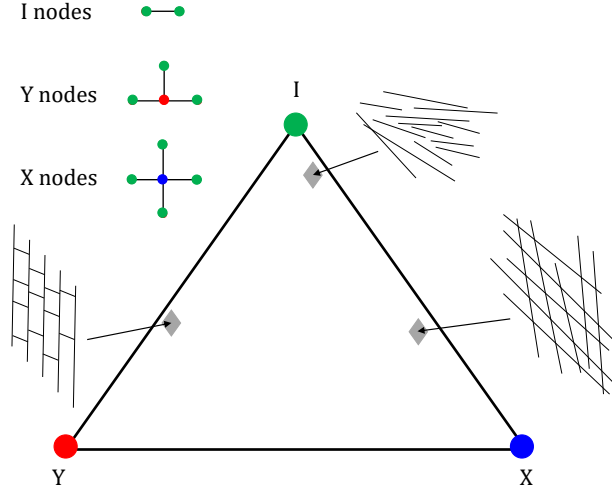


**Figure 3.** Illustration of topology in fracture networks. After Sanderson and Nixon (2015).

302

## 2.4 Preprocessing algorithm

303

304

305

306

307

308

309

310

311

312

313

314

For an accurate and efficient graph-based approach, a correct graph representation of the fracture network is necessary. Since not all intersections are always given via the fracture network’s geological (or automatic) interpretation, we need to calculate all the intersections to construct the correct graph for a fracture network. After finding all the intersections, the large fractures are partitioned into smaller fracture segments with length  $l_f$ . Then, any two nodes that are too close in proximity are merged. Subsequently, segments that intersect at an angle below a certain threshold denoted as  $\theta_{a,min}$  are merged as well. Furthermore, an optional straightening of the fractures can be applied to simplify the meshing procedure further if fractures intersect within  $[180-\theta_{s,min}, 180+\theta_{s,min}]$ . These steps are illustrated in Figure 4 and thoroughly explained in the following sections. Lastly, an aperture correction procedure is proposed, which deals with variable apertures and connecting previously disconnected fractures.

315

### 2.4.1 Intersections

316

317

318

319

320

Here the intersection detection method is described. The intersections are found by checking all combinations of any two edges. The combinations can be found via the binomial formula. All edges are parameterized, and a  $2 \times 2$  linear system is solved for each pair of edges. Any intersection that occurs splits the two edges into four, and a vertex is added.

321

322

323

324

325

326

327

328

Let  $\mathcal{X} = V \in \mathbb{R}^{n \times d}$  be the set of coordinates in the physical space of all unique vertices in the graph, where  $n$  is the number of vertices and  $d$  is the dimension of the physical space associated with the graph (i.e., fracture network). Then, let  $\mathcal{P} = E \in \mathbb{R}^{m \times 2}$  be the set of all edges in the graph, where  $m$  is the number of edges and 2 represents the number of vertices associated with each edge. In other words, the  $j$ -th element of  $\mathcal{P}$ ,  $p_j \in \mathbb{N}^{2 \times 1}$ , represents the set of two natural numbers associated with the two vertices of edge  $j$ . This means that  $\mathcal{X}(p_j^1) = V(p_j^1, \cdot) = \mathbf{x}_j^1$  and  $\mathcal{X}(p_j^2) = V(p_j^2, \cdot) = \mathbf{x}_j^2$ , where  $\mathbf{x}_j^1, \mathbf{x}_j^2 \in \mathbb{R}^d$  are the two vertices associated with edge  $j$ .

329

330

Finding all the intersections between any two edges, without any assumption on the location or orientation of the edge, can be done as follows. First parameterize all seg-

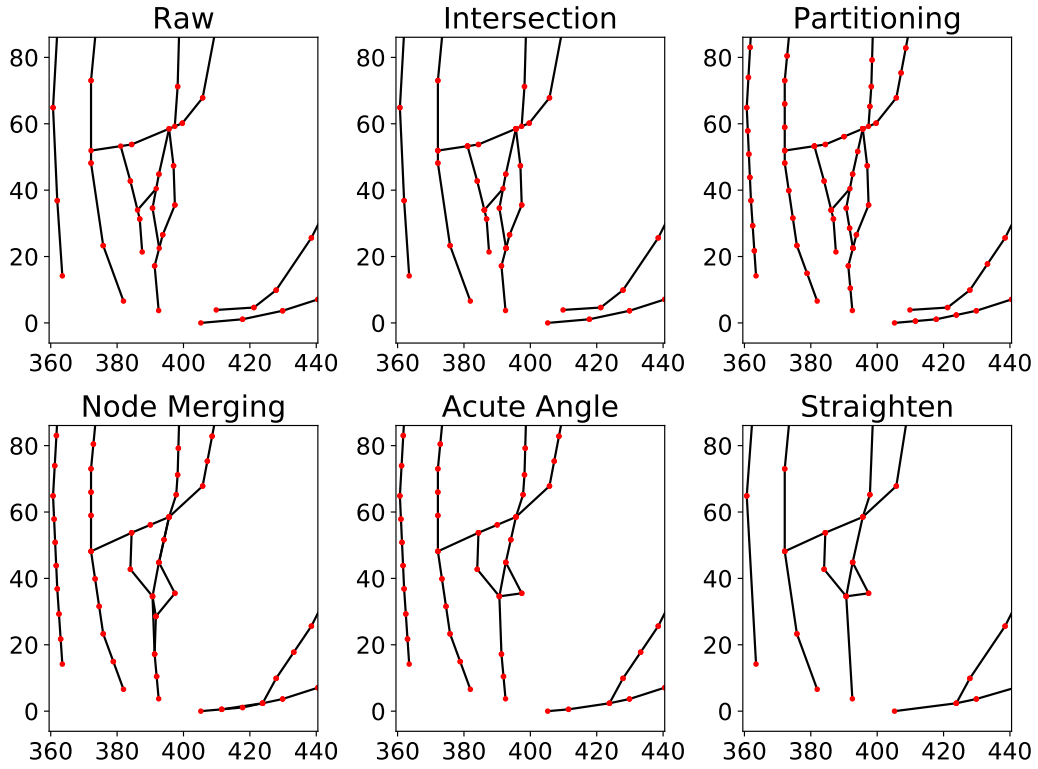


**Figure 4.** Illustration of the steps in the preprocessing workflow, from the raw data to a fully processed fracture network. The partitioning and node merging steps are a function of  $l_f$  while the acute angle and straighten steps are a function of  $\theta_{a,min}$  and  $\theta_{s,min}$  respectively. The smaller the  $l_f$ , the more precise the preprocessed network represents the raw data. However, small  $l_f$  means that the subsequent steps in the algorithm take substantially more time.

331 ments, using the following equation:

$$332 \quad \mathbf{r}_j(t) = \mathbf{x}_j^1 + t(\mathbf{x}_j^2 - \mathbf{x}_j^1), \quad j = 1, \dots, m, \quad (4)$$

333 where  $\mathbf{r}_j(t)$  represents a point on the fracture segments and  $t$  varies from 0 to 1 (from  
334 both end-points of the fracture segment). Find the pairs/combinations of edges,  $(i, j)$ ,  
335 that can possibly intersect,

$$336 \quad \binom{m}{2} = \frac{(m)^2}{2}, \quad (5)$$

337 and solve the following equation for each such combination

$$338 \quad \mathbf{r}_j(t) = \mathbf{r}_i(s). \quad (6)$$

339 The two edges intersect directly whenever  $0 < t, s < 1$  is true (note:  $<$  instead  
340 of  $\leq$  indicates that the intersections at the end-points of segments are excluded). This  
341 simplifies to solving a  $2 \times d$  system of equations for each intersection, such as

$$342 \quad A\mathbf{x} = \mathbf{b}, \quad (7)$$

343 where  $A = [\mathbf{x}_i^2 - \mathbf{x}_i^1, -(\mathbf{x}_j^2 - \mathbf{x}_j^1)]$ ,  $\mathbf{x} = [t, s]^T$ , and  $\mathbf{b} = [\mathbf{x}_i^1 - \mathbf{x}_j^1]$ .

344 The actual point of intersection is calculated by plugging the  $t$  that is obtained from  
345 Equation 7 into Equation 4. Every intersection involves exactly two segments, and the  
346 intersection id for those segments and x- and y-coordinate are stored in an array. Af-  
347 ter all the segments have been checked, a loop over this array allows us to manipulate  
348 intersections accordingly. For  $\mathcal{X}$ , this amounts to  $n_{int}$  new points, where  $n_{int}$  refers the  
349 the total number of intersection points. And for  $\mathcal{P}$ , each  $p_j \in \mathcal{P}$  that contains at least  
350 one intersection gets replaced by  $n_{int}^j + 1$  new segments, where  $n_{int}^j$  refers to the num-  
351 ber of intersections on the  $j$ -th segment.

352 This naive way of finding the intersection has the downside of having a large com-  
353 putational complexity (as indicated above). To circumvent this, we applied a method  
354 that takes advantage of the fact that most time is spent solving the linear  $2 \times 2$  system  
355 in Equation 7. A simple check is applied for each pair of fracture segments to indicate  
356 if there can exist an intersection or not. Assuming the vertices of each edge (i.e., frac-  
357 ture) are ordered from smallest x-coordinate to largest, two edges can only have a pos-  
358 sible intersection if the smallest x-coordinate of one of the two edges is smaller than the  
359 largest x-coordinate of the other edge (and vice versa for the y-coordinate). This signif-  
360 icantly reduces the overall computational time of the algorithm as shown in the results  
361 section. Further reduction in computational time is achieved by parallelizing the algo-  
362 rithm, which is our ongoing development.

#### 363 **2.4.2 Node merging**

364 The node merging algorithm, in essence, is sequential. Each vertex (i.e., node) is  
365 added to the domain ~~that~~ if it doesn't violate the algebraic constraint. This means that  
366 the distance between the newly added node and any other node already in the domain  
367 must be larger than  $l_f \cdot h$ , the node is merged into the closest node already in the do-  
368 main. Parameter  $l_f$  refers to the accuracy at which the original fracture network will be  
369 processed and subsequently influences the optimal grid resolution, while  $h$  is a scaling  
370 parameter on the closed interval  $[0.5, 0.86]$ . The larger  $h$  is, the more simplified the re-  
371 sulting network becomes. Here, 0.5 is chosen as a lower bound such that any point on  
372 a fracture segment will get merged into one of the endpoints, while 0.86 is chosen as an  
373 upper bound such that any vertex perpendicular to the fracture segment with a distance  
374 equal to the height of an equilateral triangle with length  $l_f$  at the midpoint will get merged.  
375 The sequential nature of the algorithm implies that the order in which we add nodes to  
376 the domain affects the final result. Nodes that are added first are most likely placed in

377 their exact location. Another essential consideration is the fracture aperture, since the  
 378 conductive fractures often have a large impact on the fluid flow. Therefore, the fracture  
 379 segments are ordered based on their aperture. If a single aperture model is applied, then  
 380 segments are sorted based on the length of the fractures to minimize changes to the global  
 381 structure of the network. The larger the segment, the more critical it is for fluid flow,  
 382 hence the earlier it should be added to the domain.

383 The length of each fracture segment,  $L \in \mathbb{R}^m$ , can be calculated in the following  
 384 way:

$$385 \quad L = \begin{pmatrix} \|\mathbf{x}_1^1 - \mathbf{x}_1^2\| \\ \vdots \\ \|\mathbf{x}_m^1 - \mathbf{x}_m^2\| \end{pmatrix}. \quad (8)$$

386 Then we define the order of adding segments,  $O_{\text{segm}}$ , from largest to smallest:

$$387 \quad O_{\text{segm}} = \begin{cases} \{i \in \mathbb{N} \mid \forall l_i \in L, \quad l_i \geq l_{i+1}\}, & \text{if } a_i = a \\ \{i \in \mathbb{N} \mid \forall a_i \in A, \quad a_i \geq a_{i+1}\}, & \text{otherwise} \end{cases} \quad (9)$$

388 where  $a_i$  is the aperture of fracture segment  $i$ , and  $A$  is the list of all fracture apertures.

389 From now on, for simplicity, it is assumed that  $h = 1/2$ . This means that  $\frac{l_f}{2}$  is  
 390 the minimum distance between each vertex in the simplified graph. To achieve this, a  
 391 partitioning algorithm that divides each fracture segment in  $m_i = \max(1, \text{round}(l_i/l_f))$   
 392 subsegments is executed. See Algorithm 2 for the detailed description.

393 Now we can construct the graph representation of the ordered and partitioned fracture  
 394 network, using Algorithm 1 and substituting  $\mathcal{F}$  with  $\mathcal{F}_{\text{new}}$  and  $m$  with  $m_{\text{new}}$ . Fur-  
 395 thermore, the problem is that vertices are added to the domain and not necessarily edges.  
 396 Therefore, we need to determine the order in which vertices should be added to the do-  
 397 main. The order of the vertices,  $O_{\text{vertices}}$ , can be found with Algorithm 3.

398 After the order is determined and  $B$  and  $\mathcal{X}$  are sorted, the primary node merging  
 399 algorithm can be applied. It simply consists of sequentially checking, from highest to low-  
 400 est priority vertices, if a newly added node violates the algebraic constraint (i.e., is within  
 401  $\frac{l_f}{2}$  from any nodes already in the domain). This is thoroughly described in Algorithm 4.

402 The main parameter in the partitioning and subsequent node merging algorithm  
 403 is the preprocessing accuracy  $l_f$ . This parameter determines the minimum distance be-  
 404 tween any vertex in the simplified graph. The computational time of the algorithm scales  
 405 proportionally to the  $l_f$  and the number of fractures.

### 406 **2.4.3 Straightening and removing acute angles**

407 Another (optional) modification to the fracture network is the straightening of frac-  
 408 ture segments. This amounts to checking each vertex with order two and calculating the  
 409 angle between the two edges leaving this vertex. If this angle is within some threshold,  
 410 particularly within  $[180 - \theta_{s,\text{min}}, 180 + \theta_{s,\text{min}}]$ , the node can be removed since the frac-  
 411 ture is considered straight. The angle  $\theta_{s,\text{min}}$  is typically chosen on the interval  $[0, 7.5]$ ,  
 412 depending on how severely the user wants to straighten the fractures. The straighten-  
 413 ing of fractures can be beneficial when considering meshing tools such as GMSH (Geuzaine  
 414 & Remacle, 2009). The reason for this is that conformal meshing techniques require the  
 415 fracture to be embedded into the domain. Less embedded fractures mean faster and eas-  
 416 ier meshing.

417 Simply merging the conflicting nodes doesn't resolve all the artifacts associated with  
 418 meshing DFMs. This is mainly caused by the fact that the algebraic constraint,  $\frac{l_f}{2}$ , is  
 419 constant. Whenever nodes are merged, the corresponding edge (i.e., fracture segment)  
 420 might be stretched and have a length greater than  $l_f$ . This might result in vertices be-

421 ing placed near existing edges and not flagged as problematic nodes by the node merg-  
 422 ing algorithm. Therefore, an need an additional correction to the network is required to  
 423 obtain the optimal representation for meshing purposes.

424 The algorithm for removing the acute angles is very similar to Algorithm 5; how-  
 425 ever, now the loop is over all nodes with a degree bigger than one. Instead of calculat-  
 426 ing one angle,  $\binom{d_i}{2}$  angles are computed between all edges leaving the vertex  $i$ , where  $d_i$   
 427 is the degree of vertex  $i$ . The two edges corresponding to the smallest angle below a cer-  
 428 tain threshold will be merged. The smaller segment will be merged in the larger segment,  
 429 and the non-coinciding vertex will be merged in the closest vertex of the larger segment.  
 430 This ensures minimal changes to the fracture network due to other possible edges leav-  
 431 ing the merged vertex. The tolerance for the minimal angle  $\theta_{a,min}$  is typically chosen  
 432 on the interval  $[0, 18]$  degrees. Larger  $\theta_{a,min}$  means a more simplified fracture network  
 433 since potentially more fracture intersections are flagged as problematic.

#### 434 2.4.4 Aperture correction

In order to incorporate low connectivity and fracture networks with variable aper-  
 tures, a fracture aperture correction is applied during the cleaning procedure. Connected  
 fractures are treated analogous to resistors in an electric circuit. Resistance is equal to  
 the inverse of the hydraulic conductivity, which in turn is a function of the square of the  
 fracture aperture. Figure 5 displays the two different corrections (Type 1 vs. Type 2).  
 Type 1 corrections result in the overlap of two segments after merging of vertices. Type  
 2 is subdivided further into 2a, which results in an edge collapse, and 2b, which connects  
 two previously disconnected edges. The following equation gives the correction for Type  
 1

$$\hat{R} = \left( \sum_{i=1}^{n=2} \frac{1}{R_i} \right)^{-1}, \quad (10)$$

where  $R_i$  is the resistance of edge  $i$  defined as

$$R_i = \frac{L_i}{a_i^2}, \quad (11)$$

where  $L_i$  is the length and  $a_i$  is the aperture of the  $i$ -th edge respectively, such that the  
 effective aperture of the corrected edge is given by

$$\hat{a} = \sqrt{\hat{L} \sum_{i=1}^{n=2} \frac{a_i^2}{L_i}}, \quad (12)$$

435 where  $\hat{L}$  is the length of the new edge.

The Type 2a correction is given by

$$\hat{R} = \sum_{i=1}^{n=2} R_i, \quad (13)$$

resulting in

$$\hat{a} = \sqrt{\frac{\hat{L}}{\sum_{i=1}^{n=2} \frac{L_i}{a_i^2}}}. \quad (14)$$

In the case of Type 2b, an effective matrix aperture is obtained by inverting the perme-  
 ability of parallel plate flow such that

$$a_{mat} = \sqrt{12k_{mat}}, \quad (15)$$

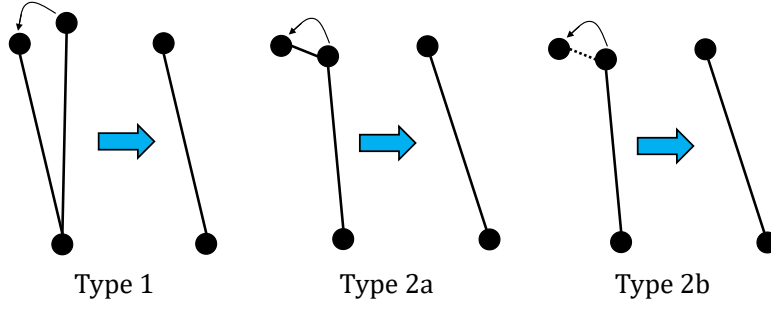


**Figure 5.** Illustration of the types of aperture corrections. Merging the non-shared vertex results in a Type 1 correction (parallel resistor), while merging the shared vertex results in a Type 2 correction (sequential resistor). An effective matrix aperture is used if the two edges are disconnected (Type 2b).

where  $k_{mat}$  is the matrix permeability at the location of the particular edge. A further addition to the Type 2b correction is added to preserve the characteristics of impermeable fractures/faults and high permeable matrix, given by

$$\hat{a} = \begin{cases} \frac{1}{\hat{L}} (a_{mat} L_{mat} + a_i L_i), & \text{if } a_{mat} > a_i \\ \frac{1}{\frac{1 - (L_i / (L_i + L_{mat}))^n}{a_i} + \frac{(L_{mat} / (L_i + L_{mat}))^n}{a_{mat}}}, & \text{if } a_{mat} \leq a_i, \end{cases} \quad (16)$$

where  $L_{mat}$  is the gap between the vertices and  $n$  is determined by fitting a least-squares solution to tracer simulation on two disconnected fractures with different gaps and characteristic cleaning lengths, given by

$$n = 9.56 \frac{L_{mat}}{L_i + L_{mat}} + 1.18. \quad (17)$$

436 If  $n \approx 1$  we have the normal harmonic mean, while  $n \rightarrow \infty$  is the same as not  
 437 applying any aperture correction. The parameter  $n$  effectively limits the aperture penalty  
 438 when connecting disconnected fractures, as it was observed from simple numerical ex-  
 439 periments that the aperture correction, in some cases, over-penalizes the effective aper-  
 440 ture. Also, note that  $n$  is bounded since  $L_{mat}$  can never exceed  $l_f h$ , since otherwise, these  
 441 vertices would not apply for merging.

442 To deal with vertices that are connected through a path in the neighborhood of the  
 443 vertices, a sub-graph is extracted around the vertex that is merged. The shortest path  
 444 is computed using Dijkstra's algorithm implementation described in Csardi et al. (2006).  
 445 Whenever there is no shortest path (i.e., even in the neighborhood the two vertices re-  
 446 main disconnected), the effective matrix aperture is used for the resistance instead. This  
 447 is represented in Figure 6

448 Figure 6 illustrates an essential feature of the aperture correction. Merging vertex  
 449 12 into vertex 11 results in a reduction of the aperture of the edges connecting vertex  
 450 10 and 12 as well as 12 and 13. This is undesirable because we want to preserve this con-  
 451 nectivity. Since the vertex merging happens sequentially, it has become evident at this  
 452 point that sorting based on aperture (highest to lowest) is more effective for an accurate  
 453 representation of fluid flow in the fracture network than simply sorting based on length.  
 454

455 All the code related to the algorithms described above is implemented in Python  
 456 and can be found at <https://github.com/MakeLikePaperrr/Fracture-Preprocessing>

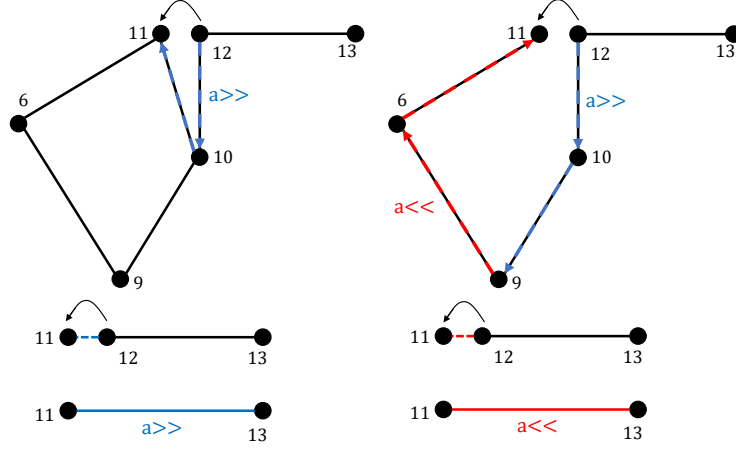


**Figure 6.** Vertices that don't share an edge might be connected through a path in the neighborhood of the vertices. A sub-graph is extracted and using Dijkstra's shortest path; the effective resistance is computed. If no shortest path exists (i.e., even in the neighborhood the two vertices remain disconnected), the effective matrix aperture is used instead.

457 **-Code.** We have made use of the following packages: NumPy (Harris et al., 2020), SciPy  
 458 (Virtanen et al., 2020), and igraph (Csardi et al., 2006).

## 459 2.5 Governing equations

460 In order to evaluate the dynamic performance of the preprocessing algorithm, several  
 461 flow scenarios are considered, for which the governing equations are specified here.  
 462 The conservation of mass, in general form, is written as

$$463 \quad \frac{\partial}{\partial t} \left( \phi \sum_{p=1}^{n_p} x_{cp} \rho_p s_p \right) + \nabla \cdot \sum_{p=1}^{n_p} x_{cp} \rho_p \mathbf{v}_p + \sum_{p=1}^{n_p} x_{cp} \rho_p q_p = 0, \quad c = 1, \dots, n_c \quad (18)$$

464 where  $\phi$  represents the porosity,  $x_{cp}$  is the molar mass fraction of component  $c$  in phase  
 465  $p$ ,  $\rho_p$  is the density,  $s_p$  is the saturation, and  $q_p$  is the source term of the  $p$ -th phase re-  
 466 spectively, and  $\mathbf{v}_p$  is the velocity of the  $p$ -th phase. The Darcy velocity of the  $p$ -th phase  
 467 is given by

$$468 \quad \mathbf{v}_p = -\frac{k_{r,p}}{\mu_p} \mathbf{K} \nabla (p_p - \rho_p \mathbf{g}), \quad p \in \{o, w\} \quad (19)$$

469 where  $k_{r,p}$  is the relative permeability,  $\mu_p$  is the viscosity and  $p_p$  is the pressure of the  
 470  $p$ -th phase respectively,  $\mathbf{K}$  is the permeability tensor, and  $\mathbf{g}$  is the directional gravita-  
 471 tional acceleration defined as  $g \nabla z$ . The equations for the tracer simulation, applied to  
 472 the variable aperture model, are obtained by having a two-component single-phase sys-  
 473 tem and setting the density and viscosity equal to unity.

474 The following equation describes the conservation of energy required for the geother-  
 475 mal simulations:

$$476 \quad \frac{\partial}{\partial t} \left( \phi \sum_{p=1}^{n_p} \rho_p s_p U_p + (1 - \phi) U_r \right) + \nabla \cdot \sum_{p=1}^{n_p} h_p \rho_p \mathbf{v}_p + \nabla (\kappa \nabla T) + \sum_{p=1}^{n_p} h_p \rho_p q_p = 0, \quad (20)$$

477 where  $U_p$  is the internal energy of fluid phase  $p$ ,  $U_r$  is the rock internal energy,  $h_p$  is the  
 478 enthalpy of phase  $p$ ,  $\kappa$  is the thermal conduction, and  $T$  is the temperature. All govern-  
 479 ing assumptions and properties can be found in (Wang et al., 2020a, 2021).

480

## 2.6 Numerical solution

481

482

483

484

485

Finite-volume discretization is applied to a general unstructured grid (using a [Two-Point Flux Approximation \(TPFA\)](#) for the fluxes across interfaces with upstream weighting) and a backward (implicit) Euler time discretization strategy to both the conservation equations and obtain the following system of equations (assuming no gravity and capillarity)

486

$$V \left[ \left( \phi \sum_{p=1}^{n_p} x_{cp} \rho_p s_p \right)^{n+1} - \left( \phi \sum_{p=1}^{n_p} x_{cp} \rho_p s_p \right)^n \right] - \Delta t \sum_l \left( \sum_{p=1}^{n_p} x_{cp}^l \rho_p^l \Gamma_p^l \Delta p^l \right) + \Delta t \sum_{p=1}^{n_p} \rho_p x_{cp} q_p = 0, \quad c = 1, \dots, n_c, \quad (21)$$

487

and

$$V \left[ \left( \phi \sum_{p=1}^{n_p} \rho_p s_p U_p + (1 - \phi) U_r \right)^{n+1} - \left( \phi \sum_{p=1}^{n_p} \rho_p s_p U_p + (1 - \phi) U_r \right)^n \right] - \Delta t \sum_l \left( \sum_{p=1}^{n_p} h_p^l \rho_p^l \Gamma_p^l \Delta p^l + \Gamma_c^l \Delta T^l \right) + \Delta t \sum_{p=1}^{n_p} h_p \rho_p q_p = 0, \quad (22)$$

488

489

490

where  $\Gamma_p^l$  is the convective and  $\Gamma_c^l$  is the thermal transmissibility of interface  $l$  and phase  $p$  respectively.

491

492

493

494

495

496

497

For details regarding the handling of the fractures, the reader is referred to [Karimi-Fard et al. \(2004\)](#). In short, fractures constitute a control volume in the computational domain of a similar dimension as the matrix control volumes, particularly approximated by a porous media where the permeability follows from the parallel plate model (cubic law, i.e.,  $k_f = a^2/12$ ). This allows solving the above system of nonlinear equations everywhere in the domain without using fracture-matrix transfer functions. The mass and heat transfer between fracture and matrix naturally follows from the discretization.

498

499

500

501

502

503

504

505

506

507

508

509

510

511

Operator-Based Linearization (OBL) is used to linearize the above system of nonlinear equations (i.e., Equation 21 and 22). OBL is a novel way of performing the linearization step. The discrete form of the mathematical equations is grouped into state-dependent operators and space-depended relations. The parameter space of the problem is discretized, where each axis is split by the uniformly distributed set of supporting points. Any point in the parameter space belongs to a certain hypercube bounded by supporting points. Next, the nonlinear operators are subsequently calculated exactly in a set of supporting points at a preprocessing stage or adaptively. At the simulation stage, the operators' values and their derivatives are evaluated using multi-linear interpolation inside a particular hyper-cube in the parameter space where the specific simulation state belongs. The multi-linear interpolation of the most nonlinear part of the governing equations provides simple, exact, and above all flexible Jacobian assemble for the nonlinear solution procedure. For details on the OBL framework, the reader is referred to [Voskov \(2017\)](#); [Khait and Voskov \(2017, 2018a\)](#).

512

513

514

515

516

517

518

519

520

The proposed fracture network processing framework has been fully integrated with the open-source [Delft Advanced Research Terra Simulator \(DARTS\)](#). DARTS is a scalable parallel simulation framework, which has been successfully applied for modeling of energy transition applications, including hydrocarbon ([Khait & Voskov, 2018b](#); [Lyu, Khait, & Voskov, 2021](#)), geothermal ([Khait & Voskov, 2018c](#); [Wang et al., 2020b](#)) and CO<sub>2</sub> sequestration ([Kala & Voskov, 2020](#); [Lyu, Voskov, & Rossen, 2021](#)) cases. The ongoing effort to include fully coupled geomechanical modeling into DARTS allowed us to directly address induced seismicity problems ([Novikov et al., 2021](#)) which is another challenge in energy transition usually directly relevant to fracture networks.

### 3 Results

This section presents the investigation of the performance of the preprocessing method described in the previous section. The performance is assessed in terms of static and dynamic qualities and is therefore subdivided accordingly. It is important to stress the difference between the preprocessing accuracy  $l_f$  and the meshing accuracy  $l_m$ . The parameter  $l_f$  refers to the minimum distance between any two vertices in the preprocessed fracture network. In contrast,  $l_m$  refers to the characteristic length of the control volumes after applying a particular meshing strategy (i.e., Frontal-Delaunay as a 2D meshing algorithm in this work, see Geuzaine and Remacle (2009) for details).

Following the definition of those two parameters, there is a significant distinction between the two preprocessing strategies described below. The first approach is defined as the “clean” strategy. In this approach, the preprocessing algorithm is executed once with a  $l_f = 1$ ,  $\theta_{a,min} = 18^\circ$ , and  $\theta_{s,min} = 2.5^\circ$ . The  $l_f$  remains unchanged in the clean strategy for subsequent coarser meshing results. The second strategy is denoted as the “optimal” strategy. In this strategy, for each subsequent coarser model, the preprocessing algorithm is executed with  $l_f = l_m$ . This means that the fracture network in the “clean” strategy remains unchanged when coarsening the mesh. In the “optimal” strategy, the fracture network changes when constructing the coarser models.

#### 3.1 Static performance of the preprocessing framework

##### 3.1.1 Changes in configuration

Figure 7 illustrates several changes to the raw fracture network after applying successive coarsening. An apparent reduction in the number of nodes (red dots) can be seen with increasing  $l_f$ , which significantly reduces the number of fracture segments. Fewer fracture segments typically indicate a lower network complexity (simply by having fewer degrees of freedom). Multilinear segments become linear (i.e., straight) because of the reduction in fracture segments, further reducing network complexity. Ultimately, small and complex features of the fracture network start to disappear while the main pattern (backbone) remains visible. The average spacing of the North-South fractures (40-50 meters) remains unchanged up to  $l_f = 32$ . Around  $l_f = 64$ , which exceeds this average spacing, the fracture configuration changes substantially, as shown in Figure 8.

##### 3.1.2 Angle distribution

A critical characteristic in fracture networks is the angle distribution, particularly weighted by the length of the fractures, especially when considering variable apertures (Baghbanan & Jing, 2008; Bisdorn et al., 2016). This usually gives an insight into the potential flow response of the network while also providing possible information on the paleostress that caused the network formation. Since multiple nodes are merged in the preprocessing approach, it is expected that these angles can change substantially when using a large  $l_f$ , where large is relative to the scale at which the raw data is collected. This can be clearly seen when looking at Figure 8. For small  $l_f$ , the deviation in angles is almost unnoticeable, while around  $l_f = 32$ , a small deviation of roughly 10% in the orientation is observed in the Whitby network. Around  $l_f = 64$ , the deviation becomes significant ( $> 20\%$ ), but the dominant orientation (N-S) is still similar to that of the raw results. Finally, at  $l_f = 128$ , the angle distribution is very different from the raw data ( $> 30\%$ ), even the dominant orientation, and doesn't resemble the original network.

Similar behavior but at earlier resolution is observed for the Brejoes network. At  $l_m = 16$  the deviation is roughly 20%. The dominant NNW-SSE orientation disappears already at  $l_f = 64$ . The average spacing of the NNW-SSE fractures in the Brejoes network is roughly 12 meters. This shorter spacing correlates with the earlier deviation in the angle distribution in the Brejoes network when compared to Whitby.

570

### 3.1.3 Topology

571

572

573

574

575

576

577

578

579

580

Besides the angle distribution, it is also important to look at connectivity and in particular, the topology changes to the fracture network. Figure 9 shows the topology of the raw and preprocessed fracture networks in the ternary topology diagram (as explained in Figure 3). A large deviation between the raw and preprocessed data is observed, even with the small  $l_f = 1$  [m]. The raw network contains roughly 55% I-nodes, 20% Y-nodes, and 25% X-nodes. The finest preprocessed network (i.e.,  $l_f = 1$  [m]) contains approximately 20% I-nodes, 75% Y-nodes, and 5% X-nodes. Furthermore, with increasing  $l_f$ , the preprocessed networks increasingly deviates towards a large X-node percentage (from 5% at  $l_f = 1$  to almost 70% at  $l_f = 128$  for Whitby and from 10% at  $l_f = 2$  to 70% at  $l_f = 64$  for Brejoes).

581

582

583

584

585

586

To illuminate the differences in topology between the fine  $l_f = 1$  and the raw data, the degree of the raw and cleaned network nodes is shown in Figure 10. Even after zooming in at the nodes of the raw network, a significant amount remains misclassified as I-nodes while they would be more suitably classified as Y-nodes or X-nodes (at this scale of observation). This is the result of two fracture segments essentially intersecting, but not exactly due to inaccuracy in image interpretation. The same behavior arises for the

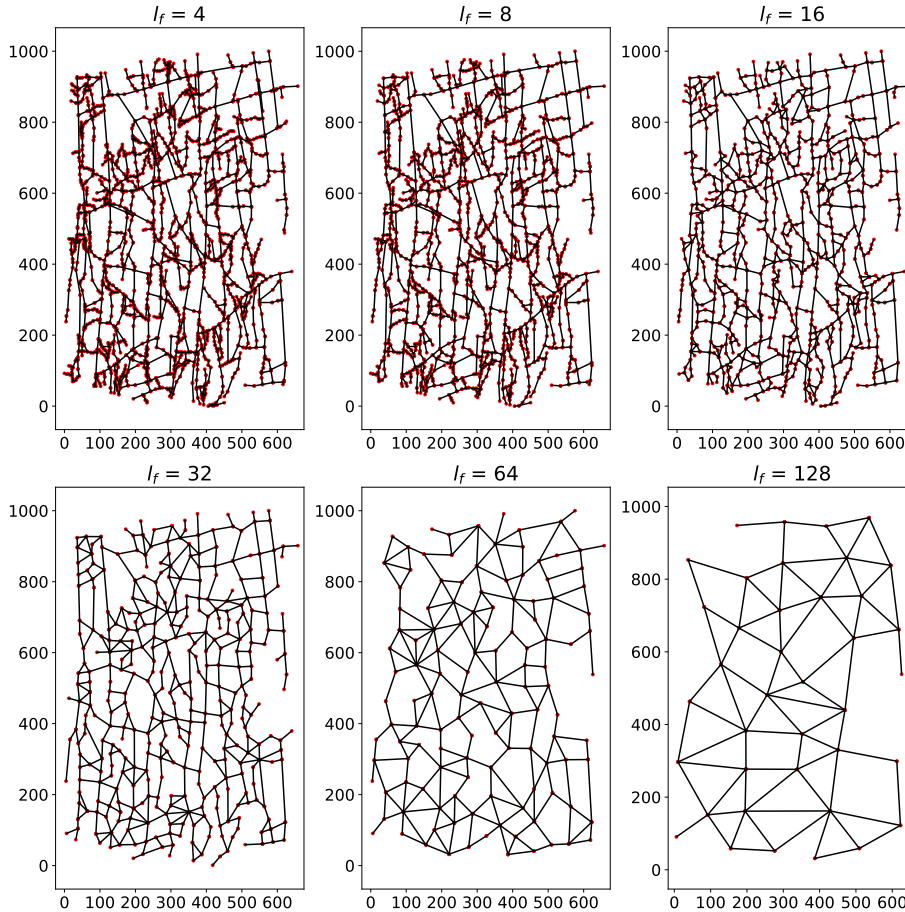


**Figure 7.** Changes to fracture network as a function of preprocessing accuracy  $l_f$ . The network's complexity is greatly reduced by the decrease in fracture segments with increasing  $l_f$ . The angles of the N-S fractures remain unchanged up to  $l_f = 64$  [m].

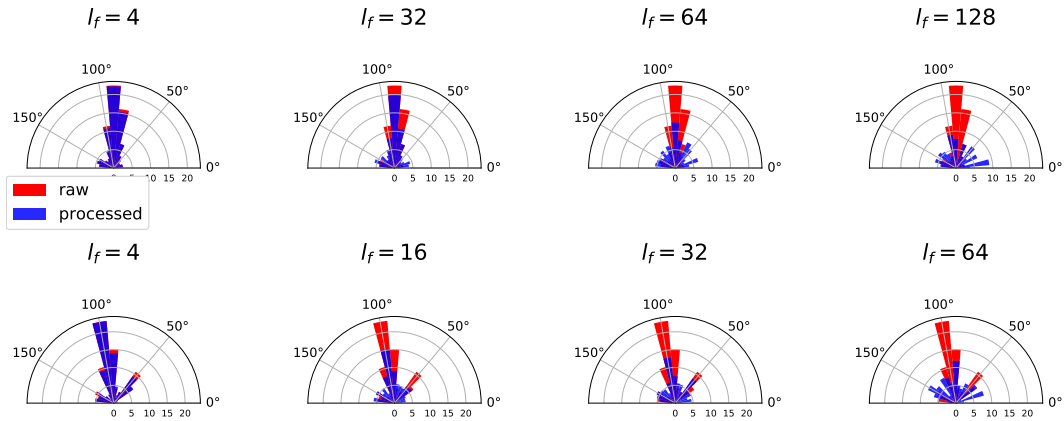


**Figure 8.** Angle distribution as a function of fracture cleaning accuracy. The top row corresponds to the Whitby network, while the bottom row corresponds to the Brejoes network. The cleaning shows no significant change between  $l_f = 4$  and  $l_f = 16$  for the Whitby network; that’s why these steps are omitted in the figure. However, the Brejoes network does show significant deviation at  $l_f = 16$ . The preprocessed Whitby network is no longer representative of the raw network at  $l_f = 128$ , while this already happens at  $l_f = 64$  for the Brejoes case.

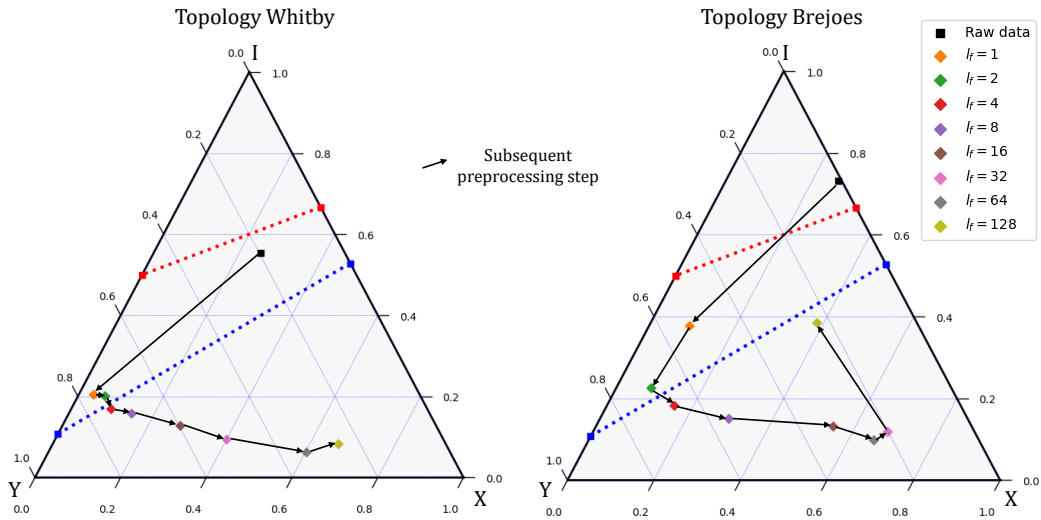


**Figure 9.** A large deviation between the raw data and the processed network’s topology in both fracture networks is observed. The reason for this is explained in Figure 10. The Brejoes network converges to the raw data for low  $l_f < 1$ . The jump in the large  $l_f = 128$  for the Brejoes case is expected due to the fracture network becoming extremely coarse. Only a few fractures actually remain, meaning the relative proportion of end-nodes greatly increases.

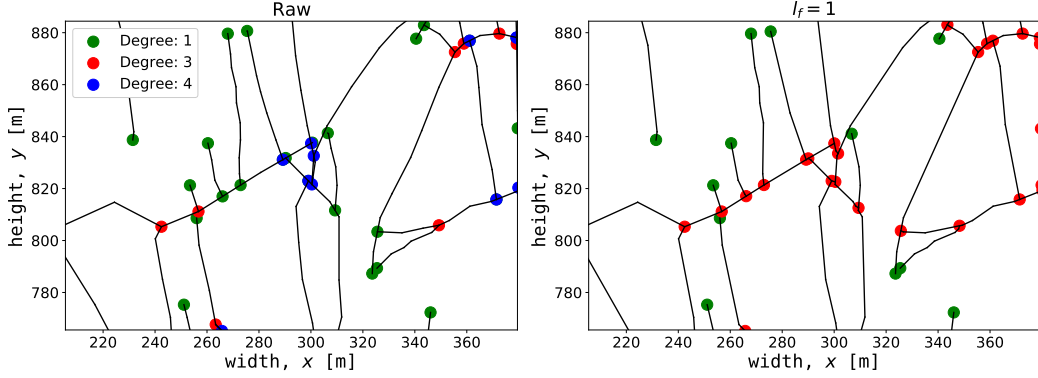


**Figure 10.** Detailed view of the fracture network topology of the Whitby network. The left image displays the raw input topology, while the right image shows the topology after applying the preprocessing algorithm with  $l_f = 1$ . Due to the manual interpretation, it can be seen that a lot of nodes are characterized as I-nodes (degree 1) or X-nodes (degree  $\geq 4$ ) in the left plot, while most seem to be Y-nodes (degree 3) (when considering usual abutment relationships in fracture mechanics and the resolution of the outcrop image).

587 X-nodes that are misclassified as Y-nodes. This happens when two fracture segments only  
 588 intersect with a minimal extension of one of the segments across the point of intersec-  
 589 tion.

### 3.1.4 Impact of changes on meshing

590  
 591 Because the complexity of the fracture network decreases, the conformal meshing  
 592 procedure becomes substantially easier. This is shown in Figure 11. A significant reduc-  
 593 tion in the number of control volumes and a more homogeneous distribution is observed  
 594 for the preprocessed meshing results compared to the raw network. The dark blue ar-  
 595 eas in the raw meshing results indicate a concentration of small control volumes. Fur-  
 596 thermore, very flat triangular elements are observed at some locations in the raw mesh-  
 597 ing results. Therefore, it seems that the volume distribution and quality of the mesh el-  
 598 ements are improved in the preprocessed results. This is quantified in Figure 12 and Fig-  
 599 ure 13 respectively. Please note that the fluid flow simulations are carried out in the 3D  
 600 domain and therefore the model is assigned a thickness (2.5D).

601 Mesh quality here refers to a similar definition as used in Mustapha and Dimitrakopou-  
 602 los (2011), particularly using the following equation

$$603 \quad q = 4\sqrt{3} \frac{A}{a + b + c}, \quad (23)$$

604 where  $A$  is the area of the triangle and  $a/b/c$  are the lengths of the three sides of the  
 605 triangle, respectively. This means that when  $q = 1$  we have a high mesh quality since  
 606 the triangle is equilateral (i.e., the optimal shape for TPFA fluid-flow simulation), while  
 607 a low-quality mesh element (i.e.,  $q \ll 1$ ) refers to a large deviation from an equilat-  
 608 eral triangle. The mesh elements in the 2.5D model are triangular prisms which means  
 609 that this mesh element quality indicator also works for this type of geometry. The rea-  
 610 son for this is that the centroid of the triangular prism lies in the same  $xy$ -plane as the  
 611 centroid of the triangle and is therefore not changing the orthogonality relationship be-  
 612 tween neighboring control volumes.

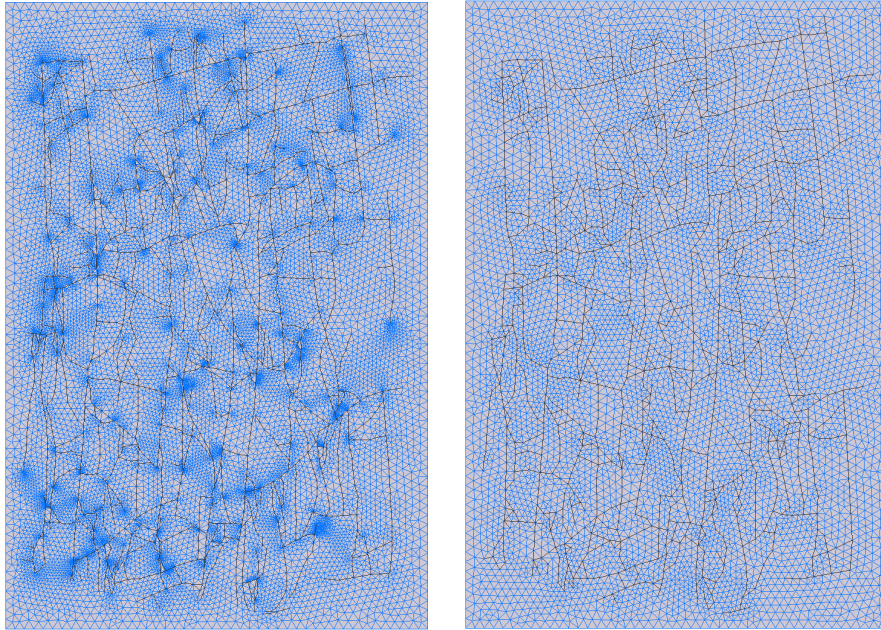


**Figure 11.** Visual comparison between the meshing result of the raw (left) versus the cleaned (right). Meshing and preprocessing accuracy are both 32 [m] (i.e.,  $l_m = l_f = 32$ ). The darker blue spots in the image on the left represent clusters of small control volumes. These appear at locations of complex fracture interactions on a scale way below the meshing resolution  $l_m$ .

613 Ultimately, the purpose of using and generating fracture networks is to utilize them  
 614 in specific industrial applications. In this work, the chosen application is geothermal en-  
 615 ergy production from the subsurface. This application usually requires multiple numer-  
 616 ical simulations to address general uncertainty in subsurface parameters. The accuracy  
 617 and speed of convergence of these simulations are highly dependent on the mesh qual-  
 618 ity and, specifically for fracture networks, the orthogonality of the control volume inter-  
 619 sections and the volume distribution. Therefore, we quantify the effect of the preprocess-  
 620 ing method on these two properties, where mesh quality is a proxy for the orthogonal-  
 621 ity of the control volume intersections. Figure 12 shows the volume distribution as a func-  
 622 tion of  $l_f$  and  $l_m$ , while Figure 13 shows the distribution of mesh element quality.

623 The volume distribution obtained after meshing the raw fracture network input is  
 624 not normally distributed. It has a peak around zero, which indicates a large number of  
 625 small control volumes. This effect becomes more substantial with increasing  $l_m$ . At  $l_m =$   
 626 32 the volume distribution of the raw network input is entirely concentrated around zero.  
 627 The volume distribution obtained after meshing the optimal preprocessed fracture net-  
 628 work input does show a normal distribution. The distribution becomes wider and more  
 629 skewed with increasing the  $l_m$ . No small control volumes are observed for the optimal  
 630 preprocessed results, even in  $l_m = 128$  [m]. The clean preprocessing strategy shows sim-  
 631 ilar behavior to the optimal strategy for small  $l_m$ , while converging to the behavior of  
 632 the raw input network for  $l_m \geq 32$ .

633 The mesh element quality obtained after meshing with a small  $l_m$  behaves simi-  
 634 larly for the raw and preprocessed input fracture data, except for a relatively small amount  
 635 of flat triangles (i.e.,  $q \approx 0$ ). An increase in the number of flat triangles (i.e.,  $q \leq 0.01$ )  
 636 from 0.32% to 1.29% and a reduction of the overall quality is observed for the raw in-  
 637 put data with increasing  $l_m$ . However, the mesh quality for the preprocessed results re-

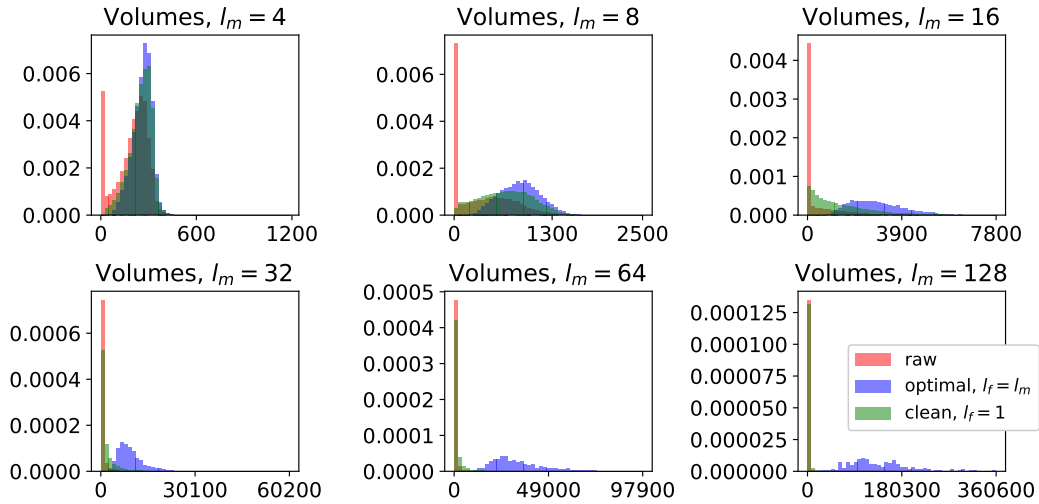


**Figure 12.** Control volume size distribution as a function of preprocessing accuracy for the Whitby network. Optimal refers to the preprocessing strategy where the fracture network is cleaned at the same accuracy as the mesh is generated. Clean refers to preprocessing the fracture network once at a small  $l_f$  and then simply decreasing the meshing resolution  $l_m$  while keeping the fracture network unchanged.

638 mains above  $q = 0.40$  even for  $l_m = 128$  [m]. Low mesh quality (i.e.,  $q \leq 0.01$ ) can be  
 639 seen as an indicator for poor simulation convergence since a few of these elements can  
 640 ruin the nonlinear convergence behavior of the numerical simulation (more than the mean  
 641 mesh element quality or the whole distribution).

## 642 3.2 Dynamic performance of preprocessing framework

### 643 3.2.1 High enthalpy single aperture

644 The dynamic performance is analyzed by applying geothermal simulation to the  
 645 different DFM models obtained after meshing (i.e., clean and optimal for different  $l_m$ ).  
 646 Geothermal simulation typically consists of a doublet system: at one point, cold water  
 647 is injected, and at another point, hot water or steam is produced. Mathematically speak-  
 648 ing, this amounts to solving Equation 18 and 20 presented in Section 2.5. The injection  
 649 point is in the bottom left of the domain, while the production point is at the top right  
 650 of the domain. Both wells are perforating a fracture segment. First, the temperature fields  
 651 of both networks are shown (Figure 14 and 15). The water saturation field is shown for  
 652 the Brejoes network (Figure 16), and finally, the temperature at the production well over  
 653 time (Figure 17).

654 The boundary conditions and modeling parameters can be found in Table 1 and  
 655 2. The simulation parameters model a situation that is investigated throughout the world  
 656 for its geothermal energy potential (Moeck, 2014). Particularly, we study geothermal en-  
 657 ergy production from a tight fractured reservoir with convective flow happening predom-  
 658 inantly through the fracture network. It is important to observe how changes to the frac-  
 659 ture network affect the simulation results in such a setup. If the fracture permeability  
 660 is much larger than the matrix permeability, the fractures will evidently play a domi-  
 661 nant role in the fluid flow patterns. There are a particular set of parameters for each net-  
 662 work. The first set of parameters simulates initially high-enthalpy single-phase super-  
 663 critical water according to IAPWS 97 equation of state (Wagner & Kretzschmar, 2008)

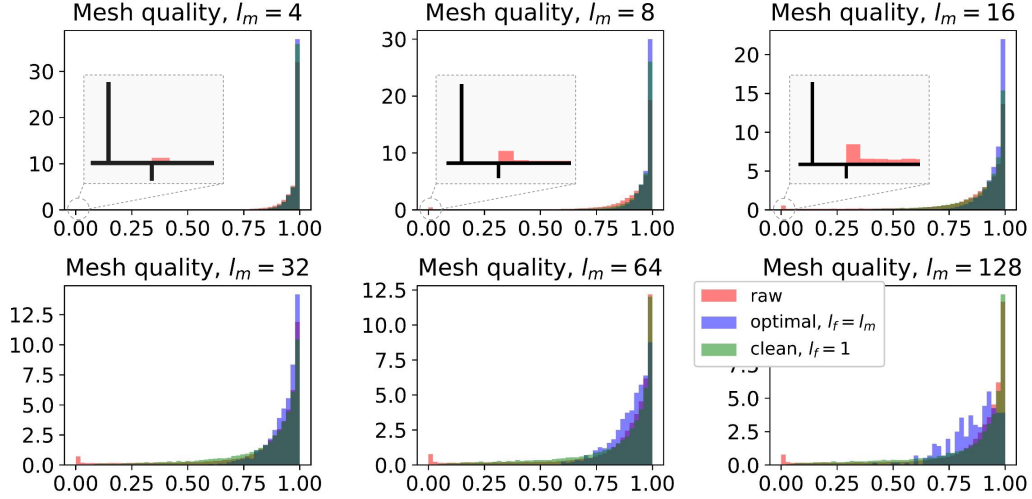


**Figure 13.** Mesh element quality distribution as a function of preprocessing accuracy for the Whitby network.

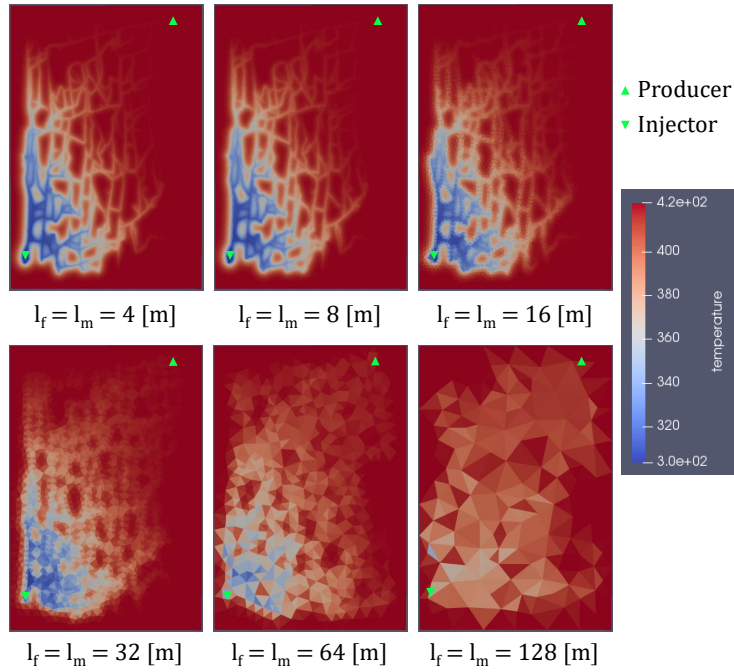
664 [used in DARTS](#). This set of parameters is applied to the Whitby case. The second set  
 665 simulates high-enthalpy steam flow conditions and is applied to the Brejoes case.

Table 1: Boundary conditions.

Parameter	Whitby	Brejoes
Rock heat conduction, $\kappa_r$ [kJ/m/day/K]	165	150
Rock heat capacity, $C_r$ [kJ/m <sup>3</sup> /K]	2500	2200
Initial pressure, $p_0$ [bar]	500	100
Initial temperature, $T_0$ [K]	423.15	583.15
Injection rate, $Q_{inj}$ [m <sup>3</sup> /day]	1000	300
Injection temperature, $T_{inj}$ [K]	303.15	308.15
Production bottom hole pressure, $p_{prod}$ [bar]	475	100

Table 2: Reservoir and simulation parameters.

Parameter	Whitby	Brejoes
Matrix permeability, $k_{mat}$ [mD]	1e-3	1e-2
Matrix porosity, $\phi_{mat}$ [-]	0.3	0.04
Fracture permeability, $k_{frac}$ [mD]	8.3e7	7.5e6
Fracture porosity, $\phi_{frac}$ [-]	1	1
Length domain, $L_x$ [m]	1050	700
Width domain, $L_y$ [m]	1050	350
Simulation time, $t$ [days]	10950	10950



**Figure 14.** Temperature distribution as a function of preprocessing and meshing accuracy for the optimal strategy after 3150 [days] (Whitby network).

666 The temperature field after 3150 [days] of simulation for the Whitby network is pre-  
 667 sented in Figure 14. The temperature is reduced near the injection point from the ini-  
 668 tial 423.15 [K] to the injection temperature of 303.15 [K]. Fluid flow primarily happens  
 669 through the fractures, hence the largest temperature variations occur closer to the frac-  
 670 tures. This is more apparent in the finer models (i.e., smaller  $l_m$ ). Larger diffusion of the  
 671 temperature profile is observed for increasing  $l_m$ . The main fracture pattern becomes  
 672 invisible at  $l_m = 64$  [m]. The temperature distribution for the Brejoes network is shown  
 673 in Figure 15. In terms of temperature distribution, a comparable trend was observed w.r.t.  
 674 to the Whitby network. The water saturation field is shown in Figure 16 after 150 days  
 675 of simulation. Accurate representation of the water saturation is more sensitive to the  
 676 resolution than temperature.

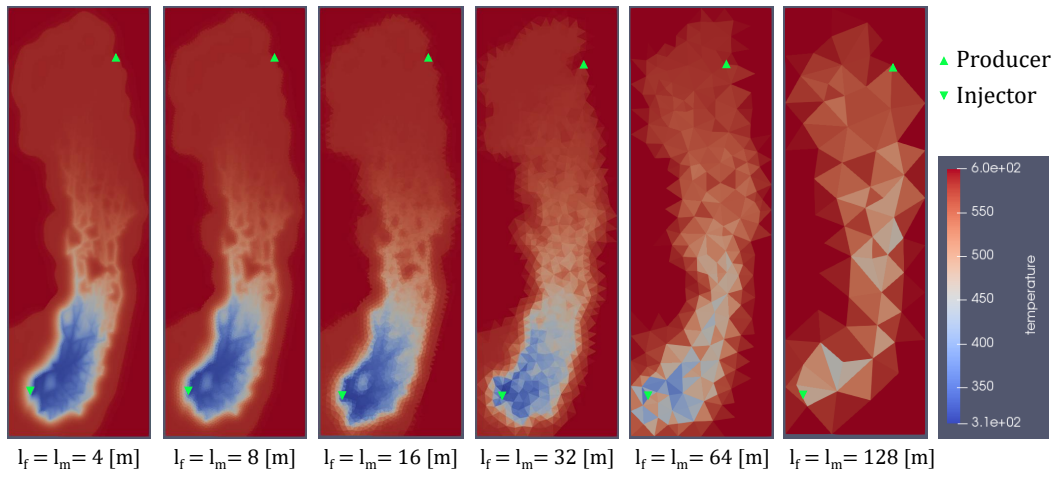


**Figure 15.** Temperature distribution as a function of preprocessing and meshing accuracy for the optimal strategy after 3150 [days] (Brejoes network).

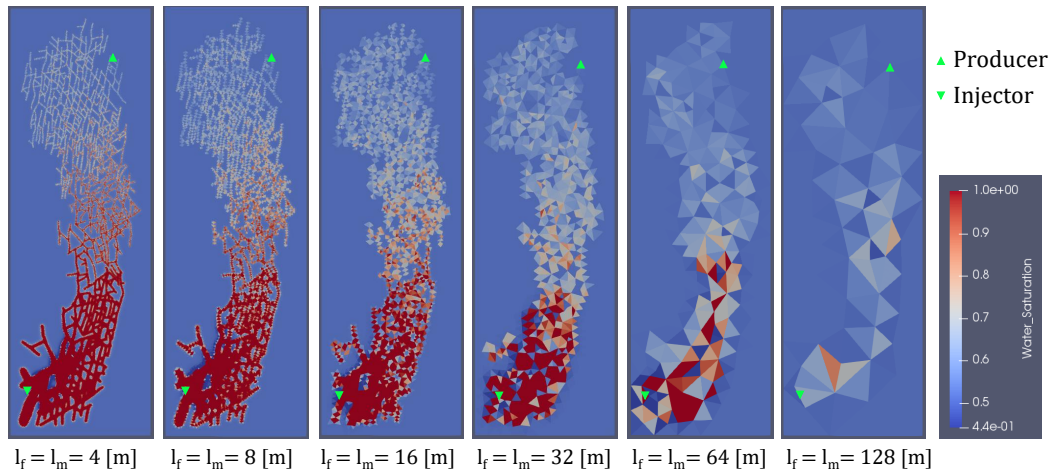


**Figure 16.** Water saturation distribution as a function of preprocessing and meshing accuracy for the optimal strategy after 150 [days] (Brejoes network).

677 The energy rate and temperature profile at the production well showed similar be-  
 678 havior; therefore, only the temperature profiles are shown in Figure 17. A commonly used  
 679 metric to analyze the flow behavior of geothermal systems is the doublet lifetime. The  
 680 lifetime is typically reached when the water temperature at the production well has de-  
 681 creased with 10-20% of the difference between initial and injection temperature. The op-  
 682 timal strategy (i.e.,  $l_f = l_m$ ) in the Whitby network starts deviating from the finer scales  
 683 at  $l_f = 32$  [m], particularly the lifetime is reduced by 670 [days]. From  $l_f = 64$  [m]  
 684 the deviation becomes more significant, notably a 2700 [days] difference in lifetime due  
 685 to early breakthrough of the cold water. At  $l_f = 128$  [m], the response does not resem-  
 686 ble the finer scales specifically the lifetime is reduced to 500 [days] due to almost instant  
 687 cold water breakthrough.

688 The clean strategy (i.e.,  $l_f = 1$  and  $l_m = l_m$ ) shows an analogous result to the  
 689 optimal strategy for the small  $l_m$ . For larger  $l_m$  the result of the clean strategy is sig-  
 690 nificantly closer to the finer scales; particularly, there is no deviation in breakthrough  
 691 times between the scales. This is expected since the fracture network is not changing (i.e.,  
 692  $l_f = 1$  for all simulations) with increasing  $l_m$ . Therefore, no changes in connectivity  
 693 or the path from injector to producer occur, which is important in this tight fractured  
 694 reservoir setting. Meshing artifacts in the clean strategy increase the number of control  
 695 volumes for larger  $l_m$ , contributing to small changes across the scales (see Table 3). The  
 696 difference between the clean and optimal strategy (i.e.,  $l_f = l_m$ ) for small  $l_m$  ( $\leq 32$ )  
 697 in terms of flow-response is negligible; however, the performance of the optimal strat-  
 698 egy is significantly better.

699 A more significant deviation in Brejoes temperature profile for the optimal case is  
 700 observed. This is in line with the other observations. This pattern is observed in the an-  
 701 gles distribution in the previous section (see Figure 8). Furthermore, Brejoes fracture den-  
 702 sity is larger (i.e., spacing between fractures is shorter), which leads to a more diffused  
 703 and less complex temperature distribution. The large connectivity also means a shorter  
 704 and highly conductive path from injector to producer, resulting in an early cold-water  
 705 breakthrough.

### 706 **3.2.2 High permeable matrix (low permeable fracture)**

707 Fractures are often seen as high-permeable conduits, but there are cases where frac-  
 708 tures or other discontinuities end up blocking fluid-flow (Gale et al., 2004). The test case  
 709 presented here consists of a single phase-steady state simulation in a reservoir with a high  
 710 permeable matrix and low permeable fractures. A small gap between the fractures ex-  
 711 ists in the middle of the domain  $(x, y) = (500, 500)$ . Since the gap exists below the mesh-  
 712 ing resolution accuracy, the preprocessing algorithm connects the fractures. In the case  
 713 of no aperture correction, the flow can only go around the fractures. With aperture cor-  
 714 rection, the preprocessed model correctly represents a similar flow pattern as in the high  
 715 fidelity model with streamlines passing through the middle of the domain.

### 716 **3.2.3 Low connectivity (variable aperture)**

717 The final test case consists of the variable aperture model applied to the Whitby  
 718 fracture network (as seen in Figure 2). Since most of the high permeable fractures (N-  
 719 S oriented) are connected through low permeable fracture (E-W oriented), this variable  
 720 aperture model results in a low connectivity fracture model. A single-phase tracer sim-  
 721 ulation shows that the aperture correction is able to preserve the low connectivity of the  
 722 network up to the numerical accuracy corresponding to the higher numerical dispersion  
 723 in the coarser model. The early breakthrough of the tracer without aperture correction  
 724 is obvious, according to Figure 2.

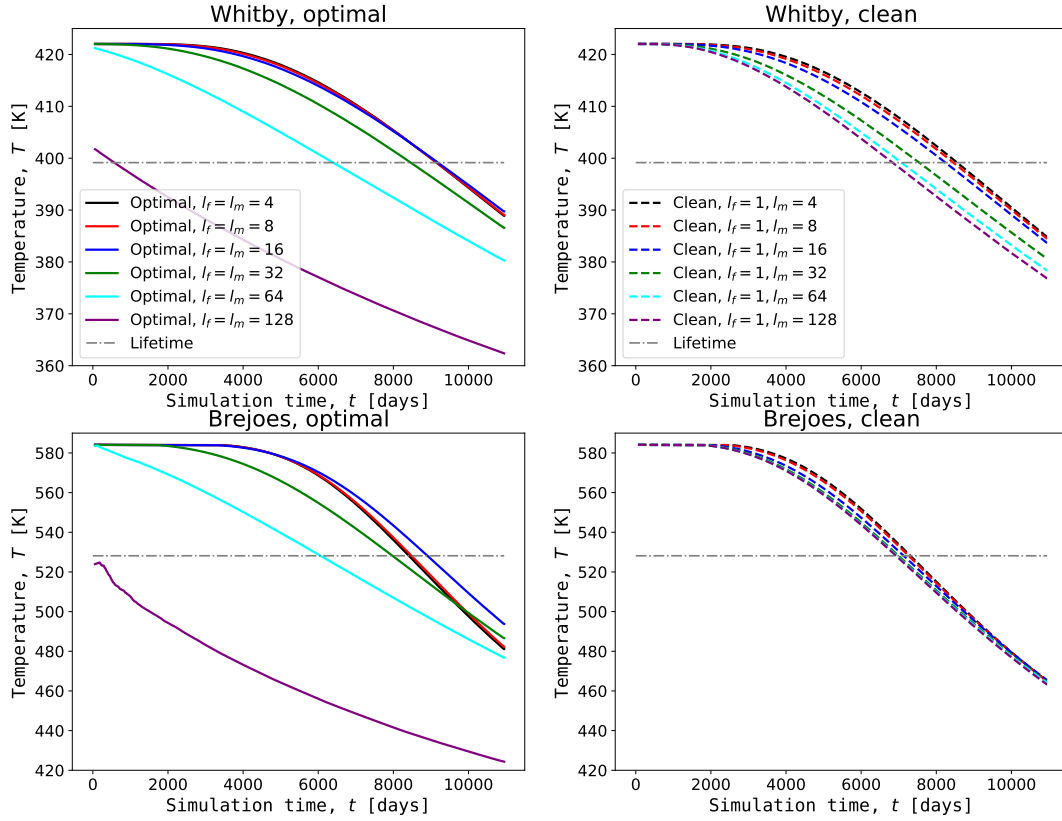


**Figure 17.** The temperature at the production well over time for optimal (left column) and clean (right column) preprocessing strategies for both the Whitby (top row) and Brejoes (bottom row) networks. Substantial deviation for large  $l_f = l_m$  in the optimal strategy was observed. This does not happen in the clean strategy. This is because the fracture network is unchanged while the mesh is coarsened. This also causes the number of control volumes to remain considerable even for large  $l_m$  thereby reducing the numerical diffusion (see Table 3 and Table 4).

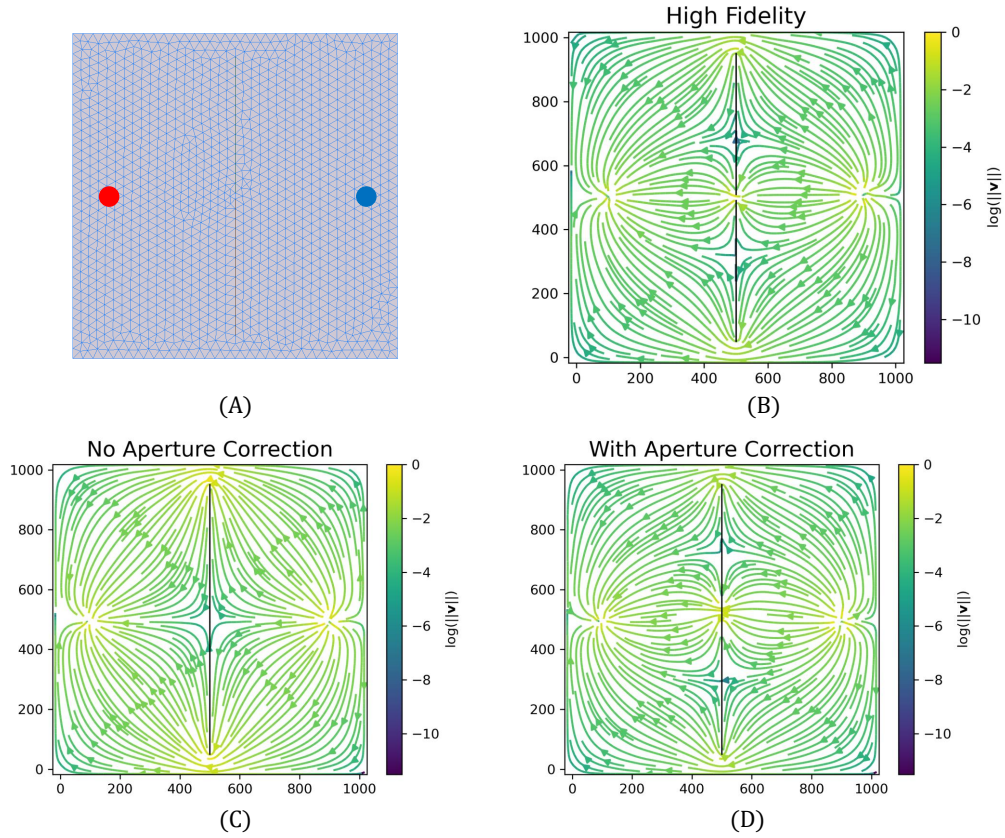


**Figure 18.** Single phase steady-state simulation of a high-permeable matrix and low permeable fractures. There is a small gap between the fractures in the high fidelity model allowing for fluid to pass. Not applying any fracture correction blocks the flow, while the aperture correction accurately depicts the high fidelity behavior.

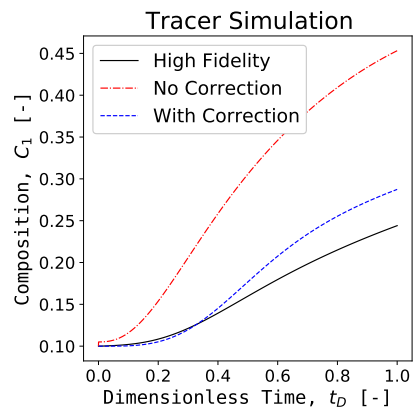


**Figure 19.** Single phase tracer simulation on the Whitby network with the variable aperture model depicted in Figure 2. A better match in breakthrough times is obtained after using the aperture correction.

**Table 3.** Numerical performance Whitby simulations.  $N_{blocks}$  corresponds to the total number of control volumes,  $N_{fracs}$  to the number of fracture control volumes,  $N_{newt}$  to the number of Newton-iterations,  $N_{lin}$  to the number of linear-iterations, and  $T_{CPU}$  to the total simulation time.  $l_f$  refers to the preprocessing accuracy, and  $l_m$  refers to the meshing accuracy.

	$N_{blocks}$	$N_{fracs}$	$N_{newt}$	$N_{lin}$	$T_{CPU}$ [s]
Clean ( $l_f = 1, l_m = 4$ )	91,780	6,800	3,543	53,210	4,159
Clean ( $l_f = 1, l_m = 8$ )	41,119	4,311	3,277	46,830	1,290
Clean ( $l_f = 1, l_m = 16$ )	24,044	3,152	3,199	40,566	538
Clean ( $l_f = 1, l_m = 32$ )	22,879	2,841	3,112	39,667	364
Clean ( $l_f = 1, l_m = 64$ )	20,142	2,824	3,087	39,340	400
Clean ( $l_f = 1, l_m = 128$ )	20,222	2,824	3,085	38,903	422
Optimal ( $l_f = l_m = 4$ )	80,672	6,362	3,436	50,573	4,079
Optimal ( $l_f = l_m = 8$ )	26,553	3,363	2,890	37,988	813
Optimal ( $l_f = l_m = 16$ )	8,718	1,594	2,680	32,600	196
Optimal ( $l_f = l_m = 32$ )	2,417	563	2,533	27,434	53
Optimal ( $l_f = l_m = 64$ )	605	147	2,395	23,119	18
Optimal ( $l_f = l_m = 128$ )	166	32	2,403	17,147	6

### 3.3 Numerical performance high enthalpy

The numerical performance of the two strategies can be found in Table 3 and Table 4 for Whitby and Brejoes, respectively. No timestep cuts are observed in both strategies for the Whitby simulations. However, several timestep cuts were observed in both strategies for the Brejoes simulations. This is reflected in the larger amount of nonlinear and linear iterations. The convergence issues can be explained by the combination of complex two-phase physics (steam condensation) and DFM in the case of high-enthalpy two-phase flow. A more sophisticated nonlinear strategy can be utilized to limit the timestep cuts (Wang & Voskov, 2019), but the main goal of this study is to have a fair comparison between the two preprocessing strategies for the conventional nonlinear solver.

It is observed that the optimal strategy shows a better convergence in both networks. A reduction in nonlinear iterations of roughly 20% for the coarse models in the Whitby simulations is observed. In the Brejoes simulations, this reduction is almost 45%. The total CPU time for the optimal strategy in the Brejoes network increases slightly at the coarsest level due to a higher number of control volumes when the coarsest strategy is applied since the scale of the cleaning mainly constrains the meshing. For the optimal strategy at the coarsest scale, the simulation time is primarily dominated by the linearization step (i.e., construction of the operators for the OBL method) and therefore doesn't reduce below 32 seconds.

The number of control volumes  $N_{blocks}$  in the clean strategy does not drop below 48-50 thousand for Whitby and 22-26 thousand for Brejoes. This is because the fracture network, at the preprocessing accuracy of  $l_f = 1$ , is too complex for the meshing software at large  $l_m$ . The result is a substantial amount of elements with low mesh quality (see Figure 13) and no further reduction in  $N_{blocks}$  with increasing  $l_m$ . This significantly increases the computational time for the clean strategy when compared with the optimal strategy. For example, at  $l_f = l_m = 32$  the optimal strategy only takes 14.6% of the clean strategy simulation time. However, this comes at the cost of a less accurate simulation response (see Figure 17).

**Table 4.** Numerical performance Brejoes simulations.  $N_{blocks}$  corresponds to the total number of control volumes,  $N_{fracs}$  to the number of fracture control volumes,  $N_{newt}$  to the number of Newton-iterations,  $N_{lin}$  to the number of linear-iterations, and  $T_{CPU}$  to the total simulation time,  $T_{ls}$  the total linear-solver time, and  $T_{lz}$  the total linearization time (constructing operators).  $l_f$  refers to the preprocessing accuracy, and  $l_m$  refers to the meshing accuracy.

	$N_{blocks}$	$N_{fracs}$	$N_{newton}$	$N_{linear}$	$T_{CPU}$ [s]
Clean ( $l_f = 1, l_m = 4$ )	157,105	8,079	6,970	163,388	6,803
Clean ( $l_f = 1, l_m = 8$ )	58,912	4,682	4,947	87,940	1,607
Clean ( $l_f = 1, l_m = 16$ )	30,739	3,035	5,129	80,568	856
Clean ( $l_f = 1, l_m = 32$ )	22,918	2,402	4,784	77,690	766
Clean ( $l_f = 1, l_m = 64$ )	24,955	2,233	5,038	78,795	618
Clean ( $l_f = 1, l_m = 128$ )	26,127	2,211	4,851	75,687	551
Optimal ( $l_f = l_m = 4$ )	150,566	7,852	4,354	108,073	3,909
Optimal ( $l_f = l_m = 8$ )	46,811	4,115	3,308	52,374	564
Optimal ( $l_f = l_m = 16$ )	15,139	2,093	2,979	38,458	167
Optimal ( $l_f = l_m = 32$ )	4,899	967	2,747	27,698	50
Optimal ( $l_f = l_m = 64$ )	1,471	371	2,632	20,254	32
Optimal ( $l_f = l_m = 128$ )	400	122	2,562	14,203	34

## 4 Discussion

The existing preprocessing strategies described in the literature only implicitly resolve the fracture segments that intersect at a small angle via node merging. We augment this with an extra step where all the low-angle intersections are explicitly resolved and improve the volume distribution, mesh quality, and the convergence of subsequent numerical simulation. Furthermore, we presented an aperture correction technique that allows handling of realistic aperture distributions and low connected fracture networks. We also contribute a comprehensive investigation of the geometry and topology changes as a function of discretization accuracy and its effect on the dynamic reservoir behavior. Next, we discuss static and dynamic results of our study and give our recommendations.

### 4.1 Topology

The inherent bias of artificial connectivity in the coarser models is evident in the static analysis. Especially the topology is sensitive to subtle changes in the fracture network. The preprocessing method does seem to converge given that the distance in the ternary topology diagram appears to decrease with decreasing  $l_f$  (except for two jumps in the Brejoes topology data for  $l_f = 1$  and  $l_f = 128$  [m]).

The large deviation from the raw topology can be explained through several points. Manual interpretation is usually made in some software (e.g., QGIS) or on the image directly. Every fracture is interpreted as a line, and two points are connected, particularly the beginning- and end-point of the fracture. Even if the interpreter meant for the two fractures to abut against each other, beginning- or end-points are rarely placed exactly on top of the existing line. The computer processing interprets the point as I- or X-node, while the interpreter meant the node to be a Y-node. This can be omitted if some snipping tool during the interpretation is used or a semi-automated (Vasuki et al., 2014) or fully automated (Prabhakaran et al., 2019) interpretation method. However, this is not always the case as shown for two networks chosen in this study.

780 The other problem is the scale of the image. The Brejoes data set has a huge res-  
 781 olution (20 mm/pixel) (Prabhakaran et al., 2019). It can be argued that you would roughly  
 782 need 15-25 pixels to be sure about the interaction of two or more fractures due to shad-  
 783 ing, contrast, and other optical effects in the image. Considering this, it would mean that  
 784 intersection and abutment relationships cannot be interpreted at a scale smaller than  
 785 300-500 [mm] (for this particular image).

786 Furthermore, the image shows a 2D representation of the fracture network. In 3D,  
 787 fractures are represented by planes. Any deviation from perfectly vertical planes would  
 788 increase the chance of nodes classified as I-nodes turning into Y-nodes. All of this leads  
 789 to the argument that the raw network data should not be used in the topological assess-  
 790 ment of fracture networks. However, a small cleaning should be applied for the analy-  
 791 sis to provide meaningful results. This observation is similar to ? (?) (refer to Auke's  
 792 paper here with the image segmentation of grains).

## 793 4.2 Fluid flow

794 As shown in Figure 14 and 15, the predictions on flow response do not seem to be  
 795 affected by small details in the fracture network. However, they are substantially differ-  
 796 ent after successive coarsening (i.e., increasing  $l_c$ ). The main reason for the earlier wa-  
 797 ter breakthrough observed in Figure 17 can be attributed to an increase in connectiv-  
 798 ity of the fracture network (see also Figure 9). Furthermore, the shortest flow path through  
 799 the fracture network from the injector to the producer is significantly reduced in the coarser  
 800 models; hence the cold water arrives earlier. Finally, since the volume of the fractures  
 801 is unchanged, even if two fracture segments are merged, the fluid velocity through a merged  
 802 fracture is higher for the same injection rate. All of these things affect the time the wa-  
 803 ter has to heat up (i.e., recharge) and reduce the breakthrough time of the cold water  
 804 in the coarser models.

805 Even without using flow-based upscaling when coarsening the mesh (i.e., increas-  
 806 ing  $l_m$ ), the flow-response for the coarser models remains accurate (up to  $l_m = 32$  for  
 807 the Whitby simulation and up to  $l_m = 16$  for Brejoes). This implies that for a fraction  
 808 of the computational time of the high-fidelity model (i.e., 1.3% for Whitby and 4.3% for  
 809 Brejoes), we are still able to obtain a representative flow and heat transfer for this com-  
 810 plex physical process. This opens up avenues for replacing effective media models in com-  
 811 mon optimization and uncertainty quantification practices, such as Arnold et al. (2016)  
 812 and Spooner et al. (2019), with more accurate DFM models (de Hoop & Voskov, 2021).

813 The main idea is that adding a fracture to an already connected network is not nec-  
 814 essarily a problem. Connecting whole clusters that were not previously connected can  
 815 pose a significant issue and significantly affects the flow and heat transfer in the reser-  
 816 voir. To remedy this, we added a novel aperture correction that penalizes connecting frac-  
 817 ture segments that do not already share a connection. The tracer simulation applied to  
 818 the Whitby fracture network with variable aperture distribution significantly improves  
 819 the match between the coarser representation and the high-fidelity model in terms of break-  
 820 through time (see Figure 19). Furthermore, the aperture correction allows us to deal with  
 821 coarsening of sealing fractures that potentially block fluid-flow, as observed in the syn-  
 822 thetic test case in Figure 18.

823 A possible addition to the preprocessing method is keeping track of the volume changes  
 824 of the fractures. When two fracture segments are merged, the cumulative volume could  
 825 be recorded. The main benefit is that the fracture volume is preserved. The downside  
 826 is that the hydraulic conductivity (permeability) of the fracture is dependent on the square  
 827 of the aperture. This means that a cumulative volume (i.e., adding the aperture of the  
 828 two segments that are merged) results in a doubled hydraulic conductivity.

829 The networks differ mainly in terms of angles and  $C_L$ . However, it is important to  
 830 touch on the similarity between the two fracture networks used in this study: both are  
 831 quite well connected. This, in combination with the observations on the earlier water breakthrough  
 832 for coarser models, begs the question: how does the preprocessing algorithm work on networks  
 833 that are poorly connected? This question is part of our future work. The ultimate goal  
 834 is to use the presented approach for an efficient and robust uncertainty quantification  
 835 procedure in fractured reservoirs of any connectivity.

836 When you have a large number of disconnected clusters, as long as the  $l_f$  is below  
 837 the smallest distance between those clusters and below the average spacing of the fractures  
 838 that predominantly affect the fluid flow, the preprocessing should be accurate even for  
 839 very coarse models. Whenever disconnected clusters are within a small distance of each  
 840 other, this becomes more difficult. A smaller  $l_f$  should be used since clusters will become  
 841 connected while, in reality, they are not. Another remedy for this problem would be disconnecting  
 842 clusters that become connected after preprocessing. This can be achieved by accurate  
 843 bookkeeping (i.e., recording before preprocessing to which cluster a certain node belongs  
 844 and observing how this evolves when running the algorithm). The issue of not preserving  
 845 average spacing for very coarse models and thereby greatly altering the fractures' orientation  
 846 is illustrated in Figure 7 and 8.

847 In our future work, we have generated a large ensemble of varying connectivity for  
 848 future work and observe how the flow response accuracy w.r.t. fine-scale changes with  
 849 increasing  $l_f$  to shed light on this issue.

### 850 4.3 Application and recommendations

851 It seems from the study presented in this paper that the flow-response is less sen-  
 852 sitive to changes in the fracture network than initially thought. The orientation of the  
 853 fractures (i.e., angle distribution) is also less sensitive than the topology. This could serve  
 854 as a recommendation to geologists and modelers that the scale and complexity at which  
 855 the data is collected and the models are constructed is unnecessarily refined. It would  
 856 save time and improve the ambiguity of our models to set a certain interpretation scale  
 857 at which you can be certain of the intersection and abutment relationships before mak-  
 858 ing the interpretation.

859 The preprocessing method effectively extracts the backbone of a complex fracture  
 860 network. Therefore, it can be used to extract the main pattern of the network and might  
 861 be useful when generating training images for algorithms such as Bruna et al. (2019).

862 The computational time of the preprocessing is insignificant to the simulation time  
 863 of fine-scale (especially after parallelization, which is already implemented and will be  
 864 described in our future work). Even more so if new functionality is utilized, such as the  
 865 Numba Python package where functions are translated into machine code before executing  
 866 the script to speed up computations. The significant speed-up in computational time for  
 867 the coarser optimal preprocessing strategy allows for the utilization in uncertainty quantification  
 868 of fractured reservoirs. Since the main reason in uncertainty quantification is understanding  
 869 the stochastic response instead of having a single very accurate simulation response.

## 870 5 Conclusion

871 This study demonstrates a strategy to simplify complex fracture networks in terms  
 872 of flow response based on a robust preprocessing approach using graph theory. We show  
 873 that using raw fracture data for topological analysis and dynamic modeling is unwise and  
 874 that some preprocessing should be applied to investigate the patterns that exist in the  
 875 studied network. Our method simplifies the topology of the fracture network by merg-  
 876 ing fracture nodes (i.e., vertices) within a certain radius. Consequently, this amounts to

877 taking the union of the incidence matrix's rows of each vertex, thereby preserving all the  
878 connectivity within the fracture network. Furthermore, it explicitly removes problem-  
879 atic fracture intersections that occur at an angle below a certain threshold. Finally, our  
880 framework extends the current preprocessing methods, such as Mustapha and Mustapha  
881 (2007) and Karimi-Fard and Durlafsky (2016), by taking into consideration an aperture  
882 correction when vertices are merged to better preserve the original connectivity and han-  
883 dle heterogeneous aperture distributions.

884 Our preprocessing framework can create a fully conformal uniformly distributed  
885 grid for a given realistic fracture network with variable aperture at the required level of  
886 accuracy. The changes introduced by the method are analyzed in terms of geometry (i.e.,  
887 angle distribution of the fracture network), meshing results (i.e., volume and quality of  
888 the elements), and dynamic response of the reservoir when subjected to geothermal high-  
889 enthalpy production conditions. Results are analysed for two realistic fracture networks  
890 based on outcrop studies, a synthetic case with sealing fractures, and a variable aper-  
891 ture model. Topology is more affected by the preprocessing than the geometry and flow  
892 response in studied networks. The performance of our method in low connectivity networks  
893 will be a part of future research.

894 Uncertainty quantification relies on a large number of numerical simulations. The  
895 presented method decreases the computational complexity of DFM models. Therefore,  
896 our approach opens up avenues for using efficient DFM models with similar computa-  
897 tional complexity as embedded-DFM (EDFM) and even Dual-Porosity models while ac-  
898 curately capturing the discrete nature of fracture networks for uncertainty quantifica-  
899 tion and history matching purposes. This is especially true for the optimal preprocess-  
900 ing strategy where cleaning and optimizing the fracture network, including treatment  
901 of intersections, node merging, and straightening, are combined.

902 The open-source computational framework performing all the preprocessing stages  
903 can be found at <https://github.com/MakeLikePaperrr/Fracture-Preprocessing-Code>.  
904

## 6 Appendix: various algorithms for DFN preprocessing

---

### Algorithm 1 Construct graph

---

```

1:  $V = \{\}$ 
2:  $n = 0$ 
3: for  $(x_i, y_i, x_j, y_j) \in \mathcal{F}$  do
4:   if  $(x_i, y_i) \notin V$  then
5:      $V = V \cup (x_i, y_i)$ 
6:      $n += 1$ 
7:
8:   if  $(x_j, y_j) \notin V$  then
9:      $V = V \cup (x_j, y_j)$ 
10:     $n += 1$ 
11:
12:  $B = \text{zeros}(n, m)$ 
13: for  $(x_i, y_i) \in V$  do
14:    $\text{ids} = \text{find}(\forall(x_i, y_i) \in \mathcal{F}(\cdot, [1, 2]) \wedge \forall(x_i, y_i) \in \mathcal{F}(\cdot, [3, 4]))$ 
15:    $B(i, \text{ids}) = 1$ 
16:
17:  $D = \text{diag}(B\mathbf{1}_{m \times 1})$ 
18:  $A = BB^T - D$ 
19:  $L = D - A$ 

```

---



---

### Algorithm 2 Partition segments

---

```

1:  $m_{\text{new}} = \sum_i^m \max(1, \text{round}(l_i/l_f))$ 
2:  $\mathcal{F}_{\text{new}} = \text{zeros}(m_{\text{new}}, 4)$ 
3:  $\text{count} = 1$ 
4: for  $k \in O_{\text{segm}}$  do
5:    $m_k = \max(1, \text{round}(l_k/l_f))$ 
6:    $\text{ids} = [1, \dots, m_k]$ 
7:    $\mathcal{F}_{\text{new}}(\text{count} : (\text{count} + m_k), 1) = \mathcal{F}(k, 1) + (\text{ids} - 1)/m_k(\mathcal{F}(k, 3) - \mathcal{F}(k, 1))$ 
8:    $\mathcal{F}_{\text{new}}(\text{count} : (\text{count} + m_k), 2) = \mathcal{F}(k, 2) + (\text{ids} - 1)/m_k(\mathcal{F}(k, 4) - \mathcal{F}(k, 2))$ 
9:    $\mathcal{F}_{\text{new}}(\text{count} : (\text{count} + m_k), 3) = \mathcal{F}(k, 1) + \text{ids} / m_k(\mathcal{F}(k, 3) - \mathcal{F}(k, 1))$ 
10:   $\mathcal{F}_{\text{new}}(\text{count} : (\text{count} + m_k), 4) = \mathcal{F}(k, 2) + \text{ids} / m_k(\mathcal{F}(k, 4) - \mathcal{F}(k, 2))$ 
11:   $\text{count} += m_k$ 
12:
13:  $O_{\text{segm, new}} = [1, \dots, m_{\text{new}}]$  //since  $\mathcal{F}_{\text{new}}$  is already ordered now!

```

---

**Algorithm 3** Determine order vertices

---

```

1:  $B = B(\cdot, O_{\text{segm}})$  //order the columns of  $B$ 
2:  $O_{\text{vertices}} = \text{zeros}(n, 1)$ 
3:  $\text{count} = 0$ 
4: for  $k = 1$  to  $m$  do
5:    $(i, j) = \text{find}(B(\cdot, k) == 1)$ 
6:   if  $i \notin O_{\text{vertices}}$  then
7:      $\text{count} += 1$ 
8:      $O_{\text{vertices}}(\text{count}) = i$ 
9:
10:  if  $j \notin O_{\text{vertices}}$  then
11:     $\text{count} += 1$ 
12:     $O_{\text{vertices}}(\text{count}) = j$ 
13:
14:  $\mathcal{X} = \mathcal{X}(O_{\text{vertices}}, \cdot)$  //sort vertices
15:  $B = B(O_{\text{vertices}}, \cdot)$  //sort rows of incidence matrix accordingly

```

---

**Algorithm 4** Node merging

---

```

1:  $D_X = \text{pdist}(\mathcal{X})$  //pairwise symmetric  $n \times n$  distance matrix for each vertex in  $\mathcal{X}$ 
2:  $\text{mergelist} = \text{zeros}(n, 1)$ 
3: for  $k = 2$  to  $n$  do
4:    $\text{id}_{\min} = \min(\{d_{k,i} \in D_X \mid \forall i \in \mathbb{N}, i < k\})$  //closest vertex already in domain
5:   if  $D_X(k, \text{id}_{\min}) < l_f/2$  then
6:      $\text{mergelist}(k) = \text{id}_{\min}$ 
7:      $B(\text{id}_{\min}, \cdot) = B(\text{id}_{\min}, \cdot) \cup B(k, \cdot)$  //record new connections from node merging
8:      $B(k, \cdot) = 0$  //remove merged node from graph
9:      $D_X(k, \cdot) = \infty$  //reset distance from removed node
10:     $D_X(\cdot, k) = \infty$  //reset distance from removed node
11:
12:  $\text{mask} = \{i \in \mathbb{N} \mid \forall i \notin \text{mergelist}, i \leq n\}$ 
13:  $\mathcal{X} = \mathcal{X}(\text{mask})$ 
14:  $n = \text{card}(\mathcal{X})$ 
15:  $B = B(\text{mask}, \cdot)$ 
16:  $B = B(\cdot, \mathbf{1}_{1 \times n} B > 1)$  //remove “collapsed” edges
17:  $B = \text{unique}(B, \text{'cols'})$  //remove overlapping edges

```

---

**Algorithm 5** Straighten fractures

---

```

1: nodelist = { $d_i \in D(G) \mid d_i == 2$ }
2: mergelistnodes = zeros(n, 1)
3: mergelistsegms = zeros(m, 1)
4: for  $k \in$  nodelist do
5:   idsegms = nonzero( $B(k, \cdot)$ )
6:    $\mathbf{v}_1 = \mathcal{F}(\text{idsegms}(1), [1, 2]) - \mathcal{F}(\text{idsegms}(1), [3, 4])$ 
7:    $\mathbf{v}_2 = \mathcal{F}(\text{idsegms}(2), [1, 2]) - \mathcal{F}(\text{idsegms}(2), [3, 4])$ 
8:   dotproduct =  $\min(1, \max(-1, \frac{\mathbf{v}_1^T \mathbf{v}_2}{\|\mathbf{v}_1\| \|\mathbf{v}_2\|}))$ 
9:    $\theta = \arccos(\text{dotproduct})180/\pi$ 
10:  if  $\theta < \theta_{\text{tol}}$  then
11:    mergelistnodes =  $k$ 
12:     $B(k, \cdot) = 0$ 
13:    mergelistsegms = idsegms(2)
14:    idnodes = nonzero( $B(\cdot, \text{idsegms}(1)) \cup$  nonzero( $B(\cdot, \text{idsegms}(2))$ )
15:     $B(\cdot, \text{idsegms}(2)) = 0$ 
16:     $B(\text{idnodes} \neq k, \text{idsegms}(1)) = 1$ 
17:
18: // $B$  and  $\mathcal{X}$  are updated similarly to Algorithm 4 using “mergelistnodes” and
    “mergelistsegms” for the removed vertices and edges respectively

```

---

**Acknowledgments**

The project was performed with a subsidy (reference TKI2017-07-UG) from the Ministry of Economic Affairs, National schemes EZ subsidies, Top sector Energy, carried out by the Netherlands Enterprise Agency. We also want to thank Mohammed Karimi-Fard for his insightful comments and suggestions regarding the preprocessing strategy. Finally, we want to thank Alexandros Daniilidis for his valuable discussion regarding the aperture correction procedure. The data and source code is available at <https://github.com/MakeLikePaperrr/Fracture-Preprocessing-Code>.

**References**

- Acuna, J. A., & Yortsos, Y. C. (1995). Application of fractal geometry to the study of networks of fractures and their pressure transient. *Water Resources Research*, *31*(3), 527–540.
- Arnold, D., Demyanov, V., Christie, M., Bakay, A., & Gopa, K. (2016). Optimisation of decision making under uncertainty throughout field lifetime: A fractured reservoir example. *Computers & Geosciences*, *95*, 123–139.
- Baghbanan, A., & Jing, L. (2008). Stress effects on permeability in a fractured rock mass with correlated fracture length and aperture. *International journal of rock mechanics and mining sciences*, *45*(8), 1320–1334.
- Balberg, I., & Binenbaum, N. (1983). Computer study of the percolation threshold in a two-dimensional anisotropic system of conducting sticks. *Physical Review B*, *28*(7), 3799.
- Barenblatt, G. (1960). Basic concepts in the theory of seepage of homogeneous liquids in fissured rocks. *Prikl. Mat. Mekh.*, *24*(5), 852–864.
- Berre, I., Doster, F., & Keilegavlen, E. (2019). Flow in fractured porous media: a review of conceptual models and discretization approaches. *Transport in Porous Media*, *130*(1), 215–236.
- Bisdorn, K., Bertotti, G., & Nick, H. M. (2016). A geometrically based method for predicting stress-induced fracture aperture and flow in discrete fracture networks. *AAPG Bulletin*, *100*(7), 1075–1097.

- 935 Bisdom, K., Nick, H., & Bertotti, G. (2017). An integrated workflow for stress and  
 936 flow modelling using outcrop-derived discrete fracture networks. *Computers &*  
 937 *Geosciences*, *103*, 21–35.
- 938 Boersma, Q., Athmer, W., Haege, M., Etchebes, M., Haukås, J., & Bertotti, G.  
 939 (2020). Natural fault and fracture network characterization for the southern  
 940 ekofisk field: A case study integrating seismic attribute analysis with image log  
 941 interpretation. *Journal of Structural Geology*, *141*, 104197.
- 942 Boersma, Q., Prabhakaran, R., Bezerra, F. H., & Bertotti, G. (2019). Linking natu-  
 943 ral fractures to karst cave development: a case study combining drone imagery,  
 944 a natural cave network and numerical modelling. *Petroleum Geoscience*, *25*(4),  
 945 454–469.
- 946 Boersma, Q. D., Bruna, P. O., De Hoop, S., Vinci, F., Tehrani, A. M., & Bertotti,  
 947 G. (2021). The impact of natural fractures on heat extraction from tight tri-  
 948 assic sandstones in the west netherlands basin: a case study combining well,  
 949 seismic and numerical data. *Netherlands Journal of Geosciences*, *100*.
- 950 Bollobás, B. (2013). *Modern graph theory* (Vol. 184). Springer Science & Business  
 951 Media.
- 952 Bruna, P.-O., Straubhaar, J., Prabhakaran, R., Bertotti, G., Bisdom, K., Mariethoz,  
 953 G., & Meda, M. (2019). A new methodology to train fracture network simula-  
 954 tion using multiple-point statistics. *Solid Earth*, *10*(2), 537–559.
- 955 Csardi, G., Nepusz, T., et al. (2006). The igraph software package for complex net-  
 956 work research. *InterJournal, complex systems*, *1695*(5), 1–9.
- 957 de Hoop, S., & Voskov, D. (2021). Fast and robust scheme for uncertainty quan-  
 958 tification in naturally fractured reservoirs. In *Spe reservoir simulation confer-*  
 959 *ence*.
- 960 Flemisch, B., Berre, I., Boon, W., Fumagalli, A., Schwenck, N., Scotti, A., ...  
 961 Tatomir, A. (2018). Benchmarks for single-phase flow in fractured porous  
 962 media. *Advances in Water Resources*, *111*, 239–258.
- 963 Gale, J. F., Laubach, S. E., Marrett, R. A., Olson, J. E., Holder, J., & Reed, R. M.  
 964 (2004). Predicting and characterizing fractures in dolostone reservoirs: Using  
 965 the link between diagenesis and fracturing. *Geological Society, London, Special*  
 966 *Publications*, *235*(1), 177–192.
- 967 Gallyamov, E., Garipov, T., Voskov, D., & Van den Hoek, P. (2018). Discrete frac-  
 968 ture model for simulating waterflooding processes under fracturing conditions.  
 969 *International Journal for Numerical and Analytical Methods in Geomechanics*,  
 970 *42*(13), 1445–1470.
- 971 Garipov, T., Karimi-Fard, M., & Tchelepi, H. (2016). Discrete fracture model for  
 972 coupled flow and geomechanics. *Computational Geosciences*, *20*(1), 149–160.
- 973 Geiger, S., & Matthäi, S. (2014). What can we learn from high-resolution numerical  
 974 simulations of single-and multi-phase fluid flow in fractured outcrop analogues?  
 975 *Geological Society, London, Special Publications*, *374*(1), 125–144.
- 976 Geuzaine, C., & Remacle, J.-F. (2009). Gmsh: A 3-d finite element mesh gener-  
 977 ator with built-in pre-and post-processing facilities. *International journal for*  
 978 *numerical methods in engineering*, *79*(11), 1309–1331.
- 979 Gureghian, A. B. (1975). A study by the finite-element method of the influence of  
 980 fractures in confined aquifers. *Society of Petroleum Engineers Journal*, *15*(02),  
 981 181–191.
- 982 Hajibeygi, H., Karvounis, D., & Jenny, P. (2011). A hierarchical fracture model  
 983 for the iterative multiscale finite volume method. *Journal of Computational*  
 984 *Physics*, *230*(24), 8729–8743.
- 985 Harris, C. R., Millman, K. J., van der Walt, S. J., Gommers, R., Virtanen, P., Cour-  
 986 napeau, D., ... Oliphant, T. E. (2020, September). Array programming with  
 987 NumPy. *Nature*, *585*(7825), 357–362. Retrieved from [https://doi.org/](https://doi.org/10.1038/s41586-020-2649-2)  
 988 [10.1038/s41586-020-2649-2](https://doi.org/10.1038/s41586-020-2649-2) doi: 10.1038/s41586-020-2649-2
- 989 Helmig, R., et al. (1997). *Multiphase flow and transport processes in the subsurface:*

- 990 *a contribution to the modeling of hydrosystems*. Springer-Verlag.  
 991 HosseiniMehr, M., Piguave Tomala, J., Vuik, C., & Hajibeygi, H. (2020).  
 992 Projection-based embedded discrete fracture model (pedfm) on corner-  
 993 point grid geometry for subsurface flow and geothermal modeling.. doi:  
 994 10.3997/2214-4609.202035245
- 995 Houben, M., Hardebol, N., Barnhoorn, A., Boersma, Q., Carone, A., Liu, Y., ...  
 996 Drury, M. (2017). Fluid flow from matrix to fractures in early jurassic shales.  
 997 *International Journal of Coal Geology*, *175*, 26–39.
- 998 Jung, A., Fenwick, D. H., & Caers, J. (2013). Training image-based scenario mod-  
 999 eling of fractured reservoirs for flow uncertainty quantification. *Computational*  
 1000 *Geosciences*, *17*(6), 1015–1031.
- 1001 Kala, K., & Voskov, D. (2020). Element balance formulation in reactive compo-  
 1002 sitional flow and transport with parameterization technique. *Computational*  
 1003 *Geosciences*, *24*(2), 609-624. doi: 10.1007/s10596-019-9828-y
- 1004 Karimi-Fard, M., & Durlofsky, L. J. (2016). A general gridding, discretization, and  
 1005 coarsening methodology for modeling flow in porous formations with discrete  
 1006 geological features. *Advances in water resources*, *96*, 354–372.
- 1007 Karimi-Fard, M., Durlofsky, L. J., & Aziz, K. (2004). An efficient discrete-fracture  
 1008 model applicable for general-purpose reservoir simulators. *SPE journal*, *9*(02),  
 1009 227–236.
- 1010 Karimi-Fard, M., Gong, B., & Durlofsky, L. J. (2006). Generation of coarse-scale  
 1011 continuum flow models from detailed fracture characterizations. *Water re-*  
 1012 *sources research*, *42*(10).
- 1013 Khait, M., & Voskov, D. (2018a). Adaptive parameterization for solving of ther-  
 1014 mal/compositional nonlinear flow and transport with buoyancy. *SPE Journal*,  
 1015 *23*, 522-534. doi: 10.2118/182685-PA
- 1016 Khait, M., & Voskov, D. (2018b). Adaptive parameterization for solving of ther-  
 1017 mal/compositional nonlinear flow and transport with buoyancy. *SPE Journal*,  
 1018 *23*(2), 522-534. doi: 10.2118/182685-pa
- 1019 Khait, M., & Voskov, D. (2018c). Operator-based linearization for efficient model-  
 1020 ing of geothermal processes. *Geothermics*, *74*, 7-18. doi: 10.1016/j.geothermics  
 1021 .2018.01.012
- 1022 Khait, M., & Voskov, D. V. (2017). Operator-based linearization for general purpose  
 1023 reservoir simulation. *Journal of Petroleum Science and Engineering*, *157*, 990–  
 1024 998.
- 1025 Koohbor, B., Fahs, M., Hoteit, H., Doummar, J., Younes, A., & Belfort, B. (2020).  
 1026 An advanced discrete fracture model for variably saturated flow in fractured  
 1027 porous media. *Advances in Water Resources*, *140*, 103602.
- 1028 Koudina, N., Garcia, R. G., Thovert, J.-F., & Adler, P. (1998). Permeability of  
 1029 three-dimensional fracture networks. *Physical Review E*, *57*(4), 4466.
- 1030 Li, L., & Lee, S. H. (2008). Efficient field-scale simulation of black oil in a naturally  
 1031 fractured reservoir through discrete fracture networks and homogenized media.  
 1032 *SPE Reservoir evaluation & engineering*, *11*(04), 750–758.
- 1033 Li, L., & Voskov, D. (2021). A novel hybrid model for multiphase flow in complex  
 1034 multi-scale fractured systems. *Journal of Petroleum Science and Engineering*,  
 1035 *203*, 108657.
- 1036 Li, X., & Li, D. (2019). A numerical procedure for unsaturated seepage analysis in  
 1037 rock mass containing fracture networks and drainage holes. *Journal of Hydrol-*  
 1038 *ogy*, *574*, 23–34.
- 1039 Lyu, X., Khait, M., & Voskov, D. (2021). Operator-based linearization approach for  
 1040 modelling of multiphase flow with buoyancy and capillarity. *SPE Journal*. doi:  
 1041 10.2118/205378-PA
- 1042 Lyu, X., Voskov, D., & Rossen, W. R. (2021). Numerical investigations of foam-  
 1043 assisted co<sub>2</sub> storage in saline aquifers. *International journal of greenhouse gas*  
 1044 *control*.

- 1045 Mallison, B. T., Hui, M.-H., & Narr, W. (2010). Practical gridding algorithms for  
 1046 discrete fracture modeling workflows. In *Ecmor xii-12th european conference*  
 1047 *on the mathematics of oil recovery* (pp. cp-163).
- 1048 Manzocchi, T. (2002). The connectivity of two-dimensional networks of spatially cor-  
 1049 related fractures. *Water Resources Research*, *38*(9), 1–1.
- 1050 Maryška, J., Severýn, O., & Vohralík, M. (2005). Numerical simulation of fracture  
 1051 flow with a mixed-hybrid fem stochastic discrete fracture network model. *Com-  
 1052 putational Geosciences*, *8*(3), 217–234.
- 1053 Moeck, I. S. (2014). Catalog of geothermal play types based on geologic controls.  
 1054 *Renewable and Sustainable Energy Reviews*, *37*, 867–882.
- 1055 Moinfar, A., Narr, W., Hui, M.-H., Mallison, B. T., & Lee, S. H. (2011). Compar-  
 1056 ison of discrete-fracture and dual-permeability models for multiphase flow in  
 1057 naturally fractured reservoirs. In *Spe reservoir simulation symposium*.
- 1058 Mustapha, H., & Dimitrakopoulos, R. (2011). Discretizing two-dimensional com-  
 1059 plex fractured fields for incompressible two-phase flow. *International Journal  
 1060 for Numerical Methods in Fluids*, *65*(7), 764–780.
- 1061 Mustapha, H., & Mustapha, K. (2007). A new approach to simulating flow in dis-  
 1062 crete fracture networks with an optimized mesh. *SIAM Journal on Scientific  
 1063 Computing*, *29*(4), 1439–1459.
- 1064 Nejadi, S., Trivedi, J. J., & Leung, J. (2017). History matching and uncertainty  
 1065 quantification of discrete fracture network models in fractured reservoirs. *Jour-  
 1066 nal of Petroleum Science and Engineering*, *152*, 21–32.
- 1067 Novikov, A., Voskov, D., Khait, M., Hajibeygi, H., & Jansen, J. (2021). A collocated  
 1068 finite volume scheme for high-performance simulation of induced seismicity in  
 1069 geo-energy applications.. doi: 10.2118/203903-MS
- 1070 Prabhakaran, R., Bruna, P.-O., Bertotti, G., & Smeulders, D. (2019). An automated  
 1071 fracture trace detection technique using the complex shearlet transform. *Solid  
 1072 Earth*, *10*(6), 2137–2166.
- 1073 Pruess, K., & Narasimhan, T. (1982). On fluid reserves and the production of super-  
 1074 heated steam from fractured, vapor-dominated geothermal reservoirs. *Journal  
 1075 of Geophysical Research: Solid Earth*, *87*(B11), 9329–9339.
- 1076 Reichenberger, V., Jakobs, H., Bastian, P., & Helmig, R. (2006). A mixed-  
 1077 dimensional finite volume method for two-phase flow in fractured porous  
 1078 media. *Advances in water resources*, *29*(7), 1020–1036.
- 1079 Sanderson, D. J., & Nixon, C. W. (2015). The use of topology in fracture network  
 1080 characterization. *Journal of Structural Geology*, *72*, 55–66.
- 1081 Sanderson, D. J., Peacock, D. C., Nixon, C. W., & Rotevatn, A. (2019). Graph the-  
 1082 ory and the analysis of fracture networks. *Journal of Structural Geology*, *125*,  
 1083 155–165.
- 1084 Spielman, D. A. (2010). Algorithms, graph theory, and linear equations in laplacian  
 1085 matrices. In *Proceedings of the international congress of mathematicians 2010  
 1086 (icm 2010) (in 4 volumes) vol. i: Plenary lectures and ceremonies vols. ii-iv:  
 1087 Invited lectures* (pp. 2698–2722).
- 1088 Spooner, V., Geiger, S., & Arnold, D. (2019). Ranking fractured reservoir models us-  
 1089 ing flow diagnostics. In *Spe reservoir simulation conference*.
- 1090 Spooner, V., Geiger, S., & Arnold, D. (2021). Dual-porosity flow diagnostics for  
 1091 spontaneous imbibition in naturally fractured reservoirs. *Water Resources Re-  
 1092 search*, e2020WR027775.
- 1093 Tene, M., Bosma, S. B., Al Kobaisi, M. S., & Hajibeygi, H. (2017). Projection-based  
 1094 embedded discrete fracture model (pedfm). *Advances in Water Resources*, *105*,  
 1095 205–216.
- 1096 Vasuki, Y., Holden, E.-J., Kovesi, P., & Micklethwaite, S. (2014). Semi-automatic  
 1097 mapping of geological structures using uav-based photogrammetric data: An  
 1098 image analysis approach. *Computers & Geosciences*, *69*, 22–32.
- 1099 Virtanen, P., Gommers, R., Oliphant, T. E., Haberland, M., Reddy, T., Cournapeau,

- 1100 D., ... SciPy 1.0 Contributors (2020). SciPy 1.0: Fundamental Algorithms  
1101 for Scientific Computing in Python. *Nature Methods*, 17, 261–272. doi:  
1102 10.1038/s41592-019-0686-2
- 1103 Voskov, D. V. (2017). Operator-based linearization approach for modeling of mul-  
1104 ti-phase multi-component flow in porous media. *Journal of Computational*  
1105 *Physics*, 337, 275–288.
- 1106 Wagner, W., & Kretzschmar, H.-J. (2008). *International steam tables: Properties*  
1107 *of water and steam based on the industrial formulation iapws-97*. Springer-  
1108 Verlag Berlin Heidelberg. Retrieved from [http://dx.doi.org/10.1007/978-3-](http://dx.doi.org/10.1007/978-3-540-74234-0)  
1109 [540-74234-0](http://dx.doi.org/10.1007/978-3-540-74234-0) doi: 10.1007/978-3-540-74234-0
- 1110 Wang, Y., de Hoop, S., Voskov, D., Bruhn, D., & Bertotti, G. (2021). Modeling  
1111 of multiphase mass and heat transfer in fractured high-enthalpy geothermal  
1112 systems with advanced discrete fracture methodology. *Advances in Water*  
1113 *Resources*, 103985.
- 1114 Wang, Y., & Voskov, D. (2019). High-enthalpy geothermal simulation with con-  
1115 tinuous localization in physics.. doi: [https://pangea.stanford.edu/ERE/pdf/](https://pangea.stanford.edu/ERE/pdf/IGASstandard/SGW/2019/Wang4.pdf)  
1116 [IGASstandard/SGW/2019/Wang4.pdf](https://pangea.stanford.edu/ERE/pdf/IGASstandard/SGW/2019/Wang4.pdf)
- 1117 Wang, Y., Voskov, D., Khait, M., & Bruhn, D. (2020a). An efficient numerical simu-  
1118 lator for geothermal simulation: A benchmark study. *Applied Energy*, 264,  
1119 114693.
- 1120 Wang, Y., Voskov, D., Khait, M., & Bruhn, D. (2020b). An efficient numerical simu-  
1121 lator for geothermal simulation: A benchmark study. *Applied Energy*, 264. doi:  
1122 10.1016/j.apenergy.2020.114693
- 1123 Warren, J., & Root, P. J. (1963). The behavior of naturally fractured reservoirs. *So-*  
1124 *ciety of Petroleum Engineers Journal*, 3(03), 245–255.
- 1125 Wellman, T. P., Shapiro, A. M., & Hill, M. C. (2009). Effects of simplifying frac-  
1126 ture network representation on inert chemical migration in fracture-controlled  
1127 aquifers. *Water Resources Research*, 45(1).
- 1128 West, D. B., et al. (2001). *Introduction to graph theory* (Vol. 2). Prentice hall Upper  
1129 Saddle River.
- 1130 Willems, C., & Nick, H. (2019). Towards optimisation of geothermal heat recovery:  
1131 An example from the west netherlands basin. *Applied energy*, 247, 582–593.
- 1132 Wong, D. L. Y., Doster, F., Geiger, S., Francot, E., & Gouth, F. (2020). Fluid flow  
1133 characterization framework for naturally fractured reservoirs using small-scale  
1134 fully explicit models. *Transport in Porous Media*, 134(2), 399–434.